The Astrophysical Journal, 938:152 (31pp), 2022 October 20 https://doi.org/10.3847/1538-4357/ac82f2

Low-frequency Radio Continuum Imaging and SED Modeling of 11 LIRGs: Radio-only and FUV to Radio Bands

Subhrata Dey[1], Arti Goyal[1], Katarzyna Małek[2], Timothy J. Galvin[3,4], Nicholas Seymour[3], Tanio Díaz Santos[5], Julia Piotrowska[1], and Vassilis Charmandaris[5,6,7]
[1] Astronomical Observatory of the Jagiellonian University, Orla 171, 30-244 Kraków, Poland; sdey@oa.uj.edu.pl
[2] National Centre for Nuclear Research, ul. Pasteura 7, 02-093 Warsaw, Poland
[3] International Centre for Radio Astronomy Research, Curtin University, Bentley, WA 6102, Australia
[4] CSIRO Space & Astronomy, PO Box 1130, Bentley WA 6102, Australia
[5] Institute of Astrophysics, Foundation for Research and Technology-Hellas, GR-71110, Heraklion, Greece
[6] Department of Physics, University of Crete, Heraklion, 71003, Greece
[7] European University Cyprus, Diogenes Street, Engomi, 1516 Nicosia, Cyprus
Received 2022 March 1; revised 2022 July 13; accepted 2022 July 15; published 2022 October 21

Abstract

We present a detailed analysis of 11 local luminous infrared galaxies from ultraviolet through far-infrared to radio (∼70 MHz to ∼15 GHz) bands. We derive the astrophysical properties through spectral energy distribution (SED) modeling using the Code Investigating GALaxy Emission (CIGALE) and UltraNest codes. The radio SEDs include our new observations at 325 and 610 MHz from the GMRT and the measurements from public archives. Our main results are (1) radio SEDs show turnovers and bends, (2) the synchrotron spectral index of the fitted radio spectra ranges between −0.5 and −1.7, and (3) the infrared luminosity, dust mass, dust temperature, stellar mass, star formation rates (SFRs), and active galactic nuclei (AGN) fraction obtained from CIGALE fall within the range exhibited by galaxies of the same class. The ratio of 60 μm infrared and 1.4 GHz radio luminosity, the 1.4 GHz thermal fraction, and emission measure range between 2.1 and 2.9, 0.1% and 10%, 0.02 and 269.5 $\times$ 10^6 cm^{-6} pc, respectively. We conclude that the turnovers seen in the radio SEDs are due to free–free absorption; this is supported by the low AGN fraction derived from the CIGALE analysis. The decomposed 1.4 GHz thermal and nonthermal radio luminosities allowed us to compute the SFR using scaling relations. A positive correlation is observed between the SFR_{IR} obtained 10 Myr ago (compared to 100 Myr ago) and 1.4 GHz radio (total and nonthermal) because similar synchrotron lifetimes are expected for typical magnetic field strengths observed in these galaxies (≈50 μG).

Unified Astronomy Thesaurus concepts: Radio continuum emission (1340); Luminous infrared galaxies (946); Spectral energy distribution (2129); Interstellar medium (847); Galaxy photometry (611)

Supporting material: figure set

1. Introduction

Characterized by a prodigious amount of emission at infrared (IR) wave bands, luminous and *ultraluminous* infrared galaxies ((U)LIRGs) dominate the IR sky. LIRGs and ULIRGs have IR luminosity in the wavelength range 8 μm $< \lambda <$ 1000 μm, L_{IR}, $\sim > 10^{11}$ $L_\odot$ and $\sim > 10^{12}$ $L_\odot$, respectively, where $L_\odot$ is the solar luminosity (Helou et al. 1988). As the name suggests, these galaxies bridge the gap between underlying astrophysical processes contributing to emission in normal star-forming galaxies and the active galactic nuclei (AGN) activity (for a review see Sanders & Mirabel 1996; Pérez-Torres et al. 2021). Their spectral energy distribution (SED), although dominated by emission at IR wave bands, ranges from radio to UV/X-rays frequencies (Yun et al. 2001; Pereira-Santaella et al. 2011), containing imprints of different astrophysical processes such as star formation, stellar evolution, chemical enrichment, processes in the interstellar medium, and the AGN (e.g., Conroy 2013). Therefore, a detailed and broadband SED modeling provides not only important constraints on astrophysical properties shaping SEDs, but also the evolutionary history of a galaxy, providing insights into the cosmic evolution of the galaxy population (Lonsdale et al. 2006).

As the radio waves remain unaffected by dust, the study of the radio continuum offers a promising approach to studying the astrophysical properties of galaxies. The q_{IR} parameter, defined as the ratio of IR (60–100 μm) to radio (1.4 GHz) luminosities, shows a surprisingly tight correlation for normal galaxies because emission at these wave bands is ascribed to a common origin and interpreted as calorimetric models (Helou et al. 1988; Condon 1992; Yun et al. 2001; Murphy 2009). In this framework, the galaxies are optically thick to UV radiation from young massive stars that are absorbed by the dust in the interstellar medium and reradiated in the far-infrared (FIR) regime. Later, these stars explode to form type II supernovae and accelerate cosmic-ray electron (CRe) that produces radio emission via a synchrotron process before escaping the galaxy (Voelk 1989). Helou et al. (1985) suggested that galaxies can be optically thin to both UV photons and cosmic rays, but coupling between gas and magnetic field should exist to maintain the radio-IR correlation (see also Lacki et al. 2010; Tabatabaei et al. 2013). Furthermore, a secondary component of the radio continuum emission due to free–free interactions between charged particles, i.e., free–free radiation, is also produced by ionization of gas in H II regions. In general, synchrotron emission is characterized by a power-law (PL) emission spectrum, $f_\nu \propto \nu^\alpha$ ($\alpha \simeq -0.8$) dominating the 1–10 GHz frequency range, whereas free–free emission has an almost flat spectrum with flux proportional

to $\nu^{-0.1}$, dominating in the frequency range $\geqslant$10 GHz (Condon 1992). The radio spectra of galaxies bend (or flatten) at lower frequencies <1 GHz due to absorption processes such as free–free absorption (FFA), synchrotron self-absorption (SSA), or the Tsytovitch–Razin effect (Israel & Mahoney 1990; Condon 1992; Clemens et al. 2010; Marvil et al. 2015).

Therefore, the exact shape of the radio spectra between the megahertz and gigahertz range depends on either the quantity and distribution of ionized (thermal) gas in galaxies (Vardoulaki et al. 2015; Clemens et al. 2008; Chyży et al. 2018; Galvin et al. 2018) or the presence of AGN (Clemens et al. 2010). Typically, the thermal fraction, TF, defined as the ratio of thermal to total emission, ranges between 0.1% and 10% at 1.4 GHz for normal star-forming galaxies and LIRGs (see Galvin et al. 2018). Therefore, constraining the radio spectrum to low frequencies is essential to understanding the absorption models for these galaxies.

Multiwavelength SED modeling, from UV to IR, provides information about the light emitted by stars, either directly or through reprocessing by the gas (emission and absorption features in the SED) and dust in the interstellar medium, while radio SED probes the nonthermal and thermal processes in galaxies (for a review see Walcher et al. 2011; Tabatabaei et al. 2017; Pérez-Torres et al. 2021). Therefore, different regimes of the broad SED provide critical insight into the nature, origin of emission, and factors that establish the energy balance. The astrophysical properties of galaxies using the Code Investigating GALaxy Emission (CIGALE) model set for main-sequence (normal) star-forming galaxies (Ciesla et al. 2017; Vika et al. 2017; Pearson et al. 2018; Riccio et al. 2021; Shirley et al. 2021), LIRGs, and ULIRGs have been characterized (Małek et al. 2017, 2018; Paspaliaris et al. 2021). As these galaxies can host AGNs, the CIGALE code includes the AGN component in the modeling. In particular, the AGN fraction (defined as the ratio of IR luminosity due to AGN and a sum of IR luminosity due to AGN and starburst), stellar mass ($M_\star$), star formation rate ($\mathrm{SFR_{IR}}$), and dust luminosity (L_{IR}), dust temperature (T_{dust}) have been obtained. The most significant finding of these studies is that LIRGs are characterized by a relatively higher $\mathrm{SFR_{IR}}$, L_{IR}, T_{dust}, and AGN fraction compared to normal star-forming galaxies and lower than those obtained by ULIRGs (Małek et al. 2017). On the other hand, detailed radio SED analysis of a large sample of galaxies is rare, primarily due to the lack of wide-area multifrequency radio surveys and targeted follow-up of suitable samples.

With this motivation, we performed a SED modeling of radio-only and far-ultraviolet (FUV) to radio bands of a sample of 11 LIRGs, including our new measurements at 325 and 610 MHz frequencies using the Giant Metrewave Radio Telescope (GMRT; Swarup 1990),[8] operated by the National Center for Radio Astronomy–Tata Institute of Fundamental Research, India. In this paper, we report the results of detailed radio SED modeling covering ∼80 MHz to ∼15 GHz and CIGALE SED modeling covering gigahertz band radio frequencies up to UV frequencies. As the CIGALE modeling cannot capture the complex shapes of low-frequency radio spectra exhibited by LIRGs and ULIRGs (e.g., Clemens et al. 2008, 2010; Galvin et al. 2018), we therefore include >1.4 GHz band radio fluxes to cover the five decades of the spectral range. Furthermore, an essential aspect of CIGALE modeling is that it works on the energy balance between UV and IR, which is ultimately related to the radio luminosity; hence, including radio fluxes in CIGALE modeling is essential for better constraining the model parameter space (in particular, the L_{dust}).

One of the primary goals of this paper is to compare the astrophysical properties resulting from SED modeling at radio-only and FUV to radio bands. The shapes of SEDs reflect the radiation laws and their parameters (such as PL energy index or emissivity) and the physical processes affecting those parameters, such as cooling or heating mechanisms in the medium. Moreover, integrated SEDs provide total energetics from different frequency regimes, and comparing those offers key information on the nature of emission and general factors that determine their energy balance principle. Furthermore, our radio SED modeling allowed us to decompose the nonthermal and thermal emission components and estimate the SFR using the basic nonthermal and thermal radio SFR calibration presented in Murphy et al. (2011) and compare them with the $\mathrm{SFR_{IR}}$ estimated from CIGALE SED modeling.

We perform detailed SED modeling of a sample of 11 nearby LIRGs (median redshift equal to 0.0181), focusing separately on radio-only and FUV-radio spectral bands. This paper is organized as follows. Sample selection is given in Section 2 while Section 3 describes data collection and analysis. Section 4 gives details of the radio-only and panchromatic (FUV to radio) SED modeling procedures. Section 5 provides the results of model fitting, i.e., characterization of the astrophysical properties of our sample. A discussion of the results obtained is given in Section 6 while the conclusion is given in Section 7.

2. Sample Selection

In this study, we have assembled a sample of 10 LIRGs with the selection criteria $\log_{10}(L_{\mathrm{IR}}) > 10.75\ L_\odot$ from the 1.425 GHz Atlas of the IRAS Bright Galaxy Sample catalog (Condon et al. 1996) and one galaxy, NGC 3508 from the 1.49 GHz Atlas of the IRAS Bright Galaxy Sample (Condon et al. 1990) of with flux densities greater than 5.24 Jy at 60 μm. These galaxies were selected based on the availability of 150 MHz data in the original release of the TIFR GMRT Sky Survey (TGSS) Data Release (DR) 4, covering 1 sr of the sky, using the GMRT (for a basic description of the survey see Sirothia 2014). We note that Intema et al. (2017) presented the entire TGSS data in their alternate data release (TGSS ADR1). Although, we selected our sample from the original TGSS DR 4 release, which had slightly better sensitivity for extended emission (rms error ∼7–9 mJy beam^{-1}) as compared to TGSS ADR1 (Intema et al. 2017), we use TGSS ADR1 integrated fluxes for radio SED fitting as its reduction and calibration methodology is fully described. The basic properties of the LIRG sample are listed in Table 1.

3. Multiwavelength Data Sets: Radio to FUV

3.1. Radio Data and AIPS Analysis

To construct the integrated radio SED for modeling, we use data in the ∼70 MHz to 15 GHz frequency range. These include our continuum observations at 325 and 610 MHz conducted using the GMRT (ID: 23_051, PI: Arti Goyal) and the publicly available archival data sets at 4.8, 8.4, and 14.5 GHz from the Karl G. Jansky Very Large Array (VLA[9]) operated by the National Radio Astronomical Observatory, USA.

[8] http://www.gmrt.ncra.tifr.res.in/

[9] https://public.nrao.edu/telescopes/vla/

Table 1
Basic Information on Our Sample of LIRGs

Name	R.A.(J2000) (h m s)	Decl.(J2000) (°′″)	z	$\log_{10}(L_{IR})$ ($L_{\odot}$)
(1)	(2)	(3)	(4)	(5)
ESO 500-G034	10 24 31.4	−23 33 10	0.0122	10.77
NGC 3508	11 02 59.7	−16 17 22	0.0128	10.65
ESO 440-IG058	12 06 51.9	−31 56 54	0.0232	11.18
ESO 507-G070	13 02 52.3	−23 55 18	0.0217	11.34
NGC 5135	13 25 44.0	−29 50 01	0.0136	11.12
IC 4280	13 32 53.4	−24 12 26	0.0162	10.85
NGC 6000	15 49 49.6	−29 23 13	0.0070	10.92
IR 16164-0746	16 19 11.8	−07 54 03	0.0271	11.29
ESO 453-G005	16 47 31.1	−29 21 22	0.0209	11.69
IR 18293-3413	18 32 41.1	−34 11 27	0.0181	11.62
ESO 593-IG008	19 14 31.1	−21 19 09	0.0485	11.77

Note. Columns: (1) source name, (2) R.A., (3) decl., (4) spectroscopic redshift from the NASA/IPAC Extragalactic Database (NED); (https://ned.ipac.caltech.edu/) (5) absolute FIR luminosity from Table 1 of Condon et al. (1996), except for NGC 3508, which is taken from Table 1 of Condon et al. (1990).

3.1.1. New GMRT Data at 325 and 610 MHz

We carried out radio continuum imaging of our sample using the GMRT at 325 and 610 MHz. The primary and phase calibrators used in our observations are provided in Table A1. We observed each target with 32 MHz bandwidth divided into 256 spectral channels. We observed standard flux calibrators at the beginning and end of the observation to calibrate the antenna gains. Phase calibrators were selected from the NRAO VLA calibrator manual list and were within 20°. Phase calibrators were observed every 30 minutes for a typical duration of 4–5 minutes to correct for antenna gain drifts, atmospheric and ionospheric gain, and phase variations. Each source was observed for a total duration of 32 minutes, in two scans consisting of 16 minutes each to enable better *U*–*V* coverage.

3.1.2. Archival VLA Data at 1.4, 4.8, 8.4, and 14.9 GHz

We analyzed the archival VLA data for galaxies wherever possible. Most galaxies in our sample were observed for a few minutes of integration time with different array configurations and different central frequencies. The data set with the largest on-source integration time was reduced when several observations were available with the same configuration and central frequency.

3.1.3. AIPS Analysis

The interferometric observations from both the GMRT and the VLA were analyzed using NRAO AIPS.[10] Data reduction was carried out in a standard fashion. The flux density scale of Baars et al. (1977) was used to obtain the flux densities of the primary (flux) calibrator, the secondary (phase) calibrator, and the target source. Antennas and baselines affected with strong radio frequency interference, nonworking antennas, were edited out after visual inspection. For the GMRT data sets, bandpass calibration was determined using the phase calibrator and the spectral channels were collapsed to generate the continuum database. Usually, spectral channels below 10 and above 200 were discarded before collapsing the data. Images were produced using task IMAGR on the channel collapsed data. To correct for distortions in the imaging, the large field of view with non-coplanar baselines (GMRT at frequencies <1 GHz), polyhedron imaging was employed where the field of view was divided into smaller fields (facets). These were 5×5 facets that covered the entire field of view up to the half power beamwidth. Usually, 3–5 rounds of phase-based self-calibration were performed iteratively by choosing point sources in the field such that the flux density is $>3\sigma$ with one synthesized beam. The final images were made with full *UV coverage* and robust weighting of 0 to weight the UV data (Briggs 1995). Facets were combined using the task FLATN. The same steps were followed for the VLA observations except that the data were obtained in two intermediate frequency (IF) channels calibrated for antenna gains before averaging them together for imaging. We did not apply any bandpass calibration since the data were obtained in a single spectral channel of 50 MHz bandwidth (BW). The final images were corrected for the reduction in sensitivity due to the shape of the antenna beam using task PBCOR with the specified parameters for the GMRT[11] and the VLA.[12]

Integrated flux densities (and uncertainty) were obtained using the task TVSTAT in AIPS for the GMRT and VLA images. We note that the synthesized beam sizes range from $\sim 0\farcs6-38''$. Assuming a typical resolution of $5''$, the linear scale is 0.5–4 kpc at the galaxy distance ($z = 0.007$–0.048). Therefore, it is reasonable to state that we obtain emissions from extended regions in most galaxies. Furthermore, we note in GMRT observations, all the proposed galaxies are detected at 610 MHz observations while LIRGs NGC 6000, IR 16164-0746, and ESO 453-G005 could not be detected at 325 MHz because the data could not be calibrated by a weak phase calibrator.

3.1.4. Radio Fluxes from the Literature

We searched for flux measurements at other frequencies along with the observations described above. In particular, we obtained measurements at the central frequencies of 74 MHz from the VLA Low-Frequency Sky Survey (VLSSr; Cohen et al. 2007), 74–231 MHz GaLactic, and Extragalactic MWA Survey (GLEAM; Wayth et al. 2015), 150 MHz TGSS ADR, 843 MHz Sydney University Molonglo Sky Survey (SUMSS; Mauch et al. 2003, 2013), 3.0 GHz VLA Sky Survey (VLASS; Lacy et al. 2020; Gordon et al. 2021) within the positional uncertainties provided by the survey parameters. For LIRGs ESO 440-IG080 and ESO 500-G034, we also included 10.0 GHz flux densities from the Australia Telescope Compact Array, published in Hill et al. (2001). For NGC 5135, we included 2.3 GHz measurements from the *S*-band Polarization All-Sky Survey (Meyers et al. 2017), and 6.7 GHz measurements from the Effelsburg telescope (Impellizzeri et al. 2008). In addition, we also included 1.4 GHz NRAO VLA Sky Survey (NVSS; Condon et al. 1998) flux for the galaxy IR 18293-3413. The GLEAM survey frequency bands are 72–103 MHz, 103–134 MHz, 139–170 MHz, 170–200 MHz, and 200–231 MHz where each band is divided into 7.68 MHz subchannels for imaging purposes (Hurley-Walker et al. 2017). The survey provides flux measurements into sub-bands of 7.68 MHz BW (each band has a frequency resolution of

[10] The National Radio Astronomy Observatory is a facility of the National Science Foundation operated under a cooperative agreement by Associated Universities, Inc.

[11] http://www.ncra.tifr.res.in:8081/~ngk/primarybeam/beam.html
[12] http://www.aips.nrao.edu/cgi-bin/ZXHLP2.PL?PBCOR

30.72 MHz), which are not independent of each other; therefore, we averaged the fluxes within each band for spectral modeling.

Table A2 summarizes the GMRT and VLA data sets analyzed by us, while Figure A1 provides total intensity radio maps overlaid on Digital Sky Survey (DSS) 2-*R*-band images in Appendix A. For radio SED modeling, we further upscaled the errors to account for variations in uncalibrated system temperature. In particular, we added in quadrature to the flux density errors an additional 10% for 150 MHz TGSS ADR1 (Intema et al. 2017), 5% for 325 and 610 MHz GMRT (Żywucka et al. 2014; Mhlahlo & Jamrozy 2021), 3% for 1.4, 4.8, 8.4, and 14.9 GHz VLA (Perley & Butler 2017), 3% for NVSS (Condon et al. 1998), 10% for VLASS (Lacy et al. 2020), 10% for GLEAM (Mhlahlo & Jamrozy 2021), 5% for SUMSS (Mauch et al. 2003; Galvin et al. 2018), 15% for Effelsberg measurements (Impellizzeri et al. 2008), 10% for *S*-PASS (Meyers et al. 2017), and 5% for ATCA (Galvin et al. 2018) measurements, respectively, as calibration error (see Equation (1) of Żywucka et al. 2014). As can be seen from Table A2 that the synthesized beam sizes for our continuum images range between a few arcseconds and 10× a few arcseconds. Because we analyzed data sets taken mostly at the B, C, and D array configurations of the VLA, it is unlikely that our galaxies are missing flux due to the lack of short *U–V* spacing data. To establish this, we compared the 1.4 GHz fluxes from Table A2 with the NVSS fluxes, obtained at a resolution of 45″. The two measurements are comparable within the measurement uncertainties. Table A3 provides the list of flux measurements used for the radio SED fitting.

3.2. UV, Optical, and IR Fluxes

We collected photometric measurements from several instruments from both ground and space-based facilities for SED modeling using CIGALE. Specifically, we obtained the fluxes from the literature by cross-matching the optical positions of our galaxies to public databases such as NED (NASA/IPAC 2019), SIMBAD (Wenger et al. 2000), VizieR (Ochsenbein et al. 2000, and NASA/IPAC Infrared Science Archive (IRSA)[13] using a matching radius of 5″–15″. This matching radius was chosen to ensure that there exists a counterpart, depending on the instrument's resolution. Specifically, the UV and optical data were collected from the NED and VizieR Photometry viewer, while the IR data were obtained from the IRSA database.

About 20–30 bands of UV-IR broadband photometry are available for these sources. They include measurements from Galaxy Evolution Explorer (GALEX), Optical/UV monitor of XMM-Newton telescope (XMM-OM), Swift ultraviolet/optical telescope, SkyMapper Southern Sky Survey (SMSS), Sloan Digital Sky Survey (SDSS) DR 16, the Two-Micron All-Sky Survey (2MASS), the Wide-field Infrared Survey Explorer (WISE), Spitzer space telescope, AKARI, and Herschel Space Observatory. Table B1 lists the instruments' characteristics. In the case of the availability of multiple flux measurements at a given wavelength, we chose the one that contained the entire galaxy. Moreover, five galaxies in our sample, namely, ESO 440-IG058, ESO 507-G070, ESO 593-IG008, IR 16164-0746, and IR 18293-3413 are either interacting, merging, or post-merging types; for these, the fluxes used in modeling include emission from the companion, too. Table B2 provides the integrated fluxes along with the integration area per band for each source used for SED modeling. For galaxies ESO 440-IG058 and NGC 5135, the IRAC apertures were optimized on a source-by-source basis to cover individual components when measuring galaxies in merger systems and to contain all the integrated flux in the case of isolated galaxies (J. M. Mazzarella et al. 2022, in preparation).

[13] https://irsa.ipac.caltech.edu/

4. SED Modeling

4.1. Radio SED

Integrated radio SEDs are modeled with physically motivated scenarios in which the radio continuum originates from either single or two emission regions characterized by the same or different populations of CRe and optical depths. Most of our adopted models are presented in Galvin et al. (2018). All modeling was performed in the observers' frame with a reference frequency, $\nu_0 = 1.4$ GHz. We consider the following models.

4.1.1. Single PL

A single PL model with emission characterized by synchrotron processes, following the form

$$S_\nu = A\left(\frac{\nu}{\nu_0}\right)^{\alpha}, \tag{1}$$

where A and α are the normalization and the spectral index, respectively, treated as free parameters.

4.1.2. Synchrotron and Free–Free Emission (SFG NC)

A radio continuum is a sum of optically thin (no curvature) synchrotron and free–free emission processes, following the form

$$S_\nu = A\left(\frac{\nu}{\nu_0}\right)^{\alpha} + B\left(\frac{\nu}{\nu_0}\right)^{-0.1}, \tag{2}$$

where A and B are the nonthermal and thermal normalization components, respectively, treated as free parameters. The free parameter, α, is the synchrotron spectral index.

4.1.3. Synchrotron and Free–Free Emission with FFA (C)

A radio continuum is a sum of optically thick synchrotron and free–free emission processes where the synchrotron emission can be suppressed due to FFA. If the frequency of this turnover due to FFA is parametrized by $\nu_{t,1}$, then the optical depth, τ, can be defined as $(\nu/\nu_{t,1})^{-2.1}$. This model has the following form:

$$S_\nu = (1 - e^{-\tau})\left[B + A\left(\frac{\nu}{\nu_{t,1}}\right)^{0.1+\alpha}\right]\left(\frac{\nu}{\nu_{t,1}}\right)^{2}, \tag{3}$$

where A and B are the nonthermal and thermal normalization components and treated as free parameters. The free parameters, $\nu_{t,1}$ and α are the turnover frequency and the synchrotron spectral index, respectively. To reduce the degeneracy of the model, we replace the term ν_0 with the turnover frequency parameter for each component. A key point here is that the models assume that the synchrotron emission is completely commingled within the extended plasma, which causes the FFA (a plasma will exhibit FFA regardless of the

physical origin of the radio photon—i.e., it does not matter what causes a radio photon to be there; it will get absorbed by the plasma).

4.1.4. Multiple FFA Components

Multiple (two) components with emission and absorption represent two star-forming regions with different orientations or compositions. The radio continuum could be complex in these cases, as these regions are integrated by large synthesized beams for unresolved galaxies. We distinguish five scenarios in the multiple components framework, which are described below: (a) radio continuum originating from two different relativistic electron populations, characterized by synchrotron spectral indices, α and α_2 in two distinct star-forming regions without FFA turnovers, labeled as SFG NC2, following the form

$$S_\nu = A\left(\frac{\nu}{\nu_0}\right)^{\alpha} + B\left(\frac{\nu}{\nu_0}\right)^{-0.1} + C\left(\frac{\nu}{\nu_0}\right)^{\alpha 2} + D\left(\frac{\nu}{\nu_0}\right)^{-0.1} \quad (4)$$

where A and C are the nonthermal normalization components, respectively, while B and D are the thermal normalization components, respectively. A, B, C, D, α, and α_2 are treated as free parameters.

(b) Radio continuum characterized by the same (single) relativistic electron population, α, in two distinct star-forming regions having different optical depths, τ_1 and τ_2, respectively, labeled as "C2 1SA":

$$S_\nu = (1 - e^{-\tau_1})\left[B + A\left(\frac{\nu}{\nu_{t,1}}\right)^{0.1+\alpha}\right]\left(\frac{\nu}{\nu_{t,1}}\right)^2 + (1 - e^{-\tau_2})\left[D + C\left(\frac{\nu}{\nu_{t,2}}\right)^{0.1+\alpha}\right]\left(\frac{\nu}{\nu_{t,2}}\right)^2, \quad (5)$$

where A and C are the nonthermal normalization components, respectively, while B and D are the thermal normalization components, respectively. A, B, C, D, α, τ_1, and τ_2 are treated as free parameters.

(c) Radio continuum characterized by the same (single) relativistic electron population, α, in two distinct star-forming regions, one without a turnover (optically thin) while the other characterized by optical depth, τ_2 (optically thick), respectively, labeled as "C2 1SAN":

$$S_\nu = \left(\frac{\nu}{\nu_0}\right)^{-2.1}\left[B + A\left(\frac{\nu}{\nu_0}\right)^{0.1+\alpha}\right]\left(\frac{\nu}{\nu_0}\right)^2 + (1 - e^{-\tau_2})\left[D + C\left(\frac{\nu}{\nu_{t,2}}\right)^{0.1+\alpha}\right]\left(\frac{\nu}{\nu_{t,2}}\right)^2, \quad (6)$$

where A and C are the nonthermal normalization components, respectively, while B and D are the thermal normalization components, respectively. A, B, C, D, α, and τ_2 are treated as free parameters. This model is most suited to explain the high-frequency kinks, elaborated in Condon & Yin (1990) and Clemens et al. (2010).

(d) Radio continuum characterized by the two different relativistic electron populations, α and α_2, in two distinct star-forming regions, one without a turnover while the other characterized by optical depth, τ_2, respectively, labeled as "C2 1SAN2":

$$S_\nu = \left(\frac{\nu}{\nu_0}\right)^{-2.1}\left[B + A\left(\frac{\nu}{\nu_0}\right)^{0.1+\alpha}\right]\left(\frac{\nu}{\nu_0}\right)^2 + (1 - e^{-\tau_2})\left[D + C\left(\frac{\nu}{\nu_{t,2}}\right)^{0.1+\alpha 2}\right]\left(\frac{\nu}{\nu_{t,2}}\right)^2, \quad (7)$$

where A and C are the nonthermal normalization components, respectively, while B and D are the thermal normalization components, respectively. A, B, C, D, α, α_2, and τ_2 are treated as free parameters.

(e) Radio continuum characterized by the two different relativistic electron populations, α and α_2, in two distinct star-forming regions, characterized by optical depths, τ_1 and τ_2, respectively, labeled as "C2".

$$S_\nu = (1 - e^{-\tau_1})\left[B + A\left(\frac{\nu}{\nu_{t,1}}\right)^{0.1+\alpha}\right]\left(\frac{\nu}{\nu_{t,1}}\right)^2 + (1 - e^{-\tau_2})\left[D + C\left(\frac{\nu}{\nu_{t,2}}\right)^{0.1+\alpha_2}\right]\left(\frac{\nu}{\nu_{t,2}}\right)^2, \quad (8)$$

where A and C are the nonthermal normalization components, respectively, while B and D are the thermal normalization components, respectively. A, B, C, D, α, α_2, τ_1 and τ_2 are treated as free parameters.

Models labeled as SFG NC2, C2 1SAN2, and C2 are motivated by a galaxy merger scenario where two distinct systems with distinct electron populations drive a new burst of star formation. For fitting the models and model comparison, we applied the Bayesian inference package called UltraNest (Buchner 2021). UltraNest works on the principle of the Monte Carlo technique called nested sampling (Skilling 2004). The advantage of nested sampling is that it allows Bayesian inference on arbitrary user-defined likelihood and provides posterior probability distributions on model parameters and marginal likelihood (*evidence*) Z. The likelihood function used in UltraNest is given as

$$\ln \mathcal{L}(\theta) = -\frac{1}{2}\sum_n \left[\frac{(D_n - f(\theta))^2}{\sigma_n^2} + \ln(2\pi\sigma_n^2)\right], \quad (9)$$

where D_n and σ_n are the vectors at n different frequencies containing flux densities and uncertainties. $f(\theta)$ represents the model fitted with the data and the parameter vector θ. For model fitting, we assume independent flux measurements with normally distributed errors, which is a prerequisite for the likelihood function used by the UltraNest. Within the Bayesian framework, the posterior distribution of any model parameter requires a prior distribution along with a likelihood function, which gives the confidence interval on the derived parameter. In our analysis, we consider a uniform prior distribution of model parameters. We constrain the priors for the normalization parameters, A, B, C, and D as positive, spectral index parameters α and α_2 in the range -0.2 and -1.8, and turnover frequencies are between 1 MHz and 50 GHz (see, for details, Galvin et al. 2018).

Table 2
An Overview of the Natural Log of the Bayes Odds Ratio from the UltraNest Fitting of Each Model to Each Source

Name	PL	SFG NC	C	SFG NC2	C2 1SA	C2 1SAN	C2 1SAN2	C2
ESO 500-G034	−68.1	−67.5	−6.3	−76.3	−1.2	0	−1.5	−4.2
NGC 3508	0	−3.5	−7.2	−8.7	−19.3	−4.6	−2.8	−7.1
ESO 440-IG058	−17.2	−14.9	0	−25.7	−3.9	−9.1	−6.8	−2.3
ESO 507-G070	−74.2	−69.9	−159.1	−21.8	−235.1	−1.9	0	−453.1
NGC 5135	−6.5	−3.7	0	−11.8	−13.0	−2.9	−35.4	−6.8
IC 4280	−3.2	−6.1	0	−12.4	−8.8	−1.6	−4.4	−0.7
NGC 6000	−3.4	0	−21.4	−6.1	−11.2	−1.6	−3.1	−408.8
IR 16164-0746	−3.4	0	−1.2	−1.3	−4.1	−0.9	−0.8	−3.0
ESO 453-G005	−2.9	0	−0.6	−3.5	−4.9	−2.1	−2.3	−1.5
IR 18293-3413	−88.7	−86.8	−90.4	−99.5	−4.3	−5.1	0	−5.1
ESO 593-IG008	−3.0	−5.9	0	−7.5	−4.3	−6.8	−3.8	−2.1

Note. In boldface, we present the most preferred model with the highest evidence value (see Equation (10)).

The evidence value is used to predict the most preferred model by calculating the Bayes odds ratio as follows:

$$\Delta\mathcal{Z} = e^{\mathcal{Z}_1 - \mathcal{Z}_2}, \tag{10}$$

where $\mathcal{Z}_1$ and $\mathcal{Z}_2$ are the evidence values for models M_1 and M_2, respectively. The strongest evidence supporting M_1 over M_2 is when $\Delta\mathcal{Z} > 150$ while for $150 > \Delta\mathcal{Z} > 20$ and $20 > \Delta\mathcal{Z} > 3$, respectively, it is either strong or positive evidence. For $\Delta\mathcal{Z} < 3$, the models are considered indistinguishable. Table 2 summarizes the natural logarithm of the Bayes odds ratio between each model and the most preferred model (Kass & Raftery 1995). This means that for a given model, $\log_e(1) = 0.0$ indicates the most preferred model. The least preferred model will have the most negative value in this representation. For each source, we provide the natural logarithm of the Bayes odds ratio for the most preferred model in boldface.

The best-fit radio SEDs are presented in Figure 1 while Table 4 gives the corresponding model parameters, along with the 1σ uncertainties corresponding to the 16th and 84th percentiles of the posterior distribution of the parameter. Our radio-only modeling separates the thermal and nonthermal components from the total emission. Using the best-fit model, we estimated total thermal(nonthermal) emission by setting the normalization of the nonthermal(thermal) component(s) to zero. Table 5 gives the total, thermal, and nonthermal fluxes at 1.4 GHz, derived from the radio-only SED modeling, along with the 1σ uncertainties corresponding to the 16th and 84th percentiles of the posterior distribution of the parameter. To assess the degeneracy caused by the number of free parameters in the best-fit model, we give corner plots for all our galaxies in Appendix (Figure A2). The complete figure set (11 images) is available in the online journal. In Figure A2, the corner plot illustrates the one- and two- dimensional projections of the posterior probability distribution of parameters. Most of our corner plots show poorly constrained thermal components, most likely due to weaker thermal emission in the frequency range covered by our data. In Table 5, we also provide the 1.4 GHz thermal fraction ($TF_{1.4}$). The TF at a given frequency is the ratio of thermal radio emission to total radio emission (synchrotron and free–free emission). NGC 3508 shows an excellent fit to the single power-law (PL) shape. Three other galaxies, NGC 6000, IR 16164-0746, and ESO 453-G005, are fitted with a single-component model without a turnover (SFG NC). The galaxies ESO 440-IG058, NGC 5135, IC 4280, and ESO 593-IG008 are fitted with the single-component model with low-frequency turnover (C). For galaxies ESO 500-G034 is best fitted with a multiple component model characterized by a single relativistic electron population in two different star-forming regions (one region with no turnover at low frequencies and the other characterized by a turnover (C2 1SAN). For galaxies ESO 507-G070 and IR 18293-3413, the best-fit model turned out to be multiple components, one characterized by different relativistic electron populations in two different star-forming regions (one region with no turnover at low frequencies and the other characterized by a turnover (C2 1SAN2). None of our galaxies fits with models described by a single relativistic electron population in two different star-forming regions with different optical depths (C2 1SA) and a multiple component model representing two different electron populations in the two distinct star-forming galaxies with different optical depths (C2).

4.2. UV to Radio SED Modeling with CIGALE

We estimate the astrophysical properties of our galaxies using the SED fitting technique with the CIGALE version 2020.0[14] (Noll et al. 2009; Boquien et al. 2019). The CIGALE modeling works on the energy balance principle, i.e., the energy emitted by dust in the mid and FIR corresponds to the energy absorbed by dust in the UV to optical range (Efstathiou & Rowan-Robinson 2003). Moreover, it uses a Bayesian-like approach to model the SED and obtains the model parameters efficiently. CIGALE is parallelized and modular, which makes it user-friendly and efficient, as it does not solve the computationally demanding radiative transfer equation (Boquien et al. 2019). It provides the best-fit model for the SED by selecting a suitable set of parameters. For this, a large grid of models is fitted to the data. The grid dimension is set by the number of input parameters used to define the different galaxy components, such as stellar emission spectra, star formation history (SFH), AGN emission, dust attenuation, nebular emission, and the slope of the radio synchrotron spectrum.

The interpretation of the observed SED is based on a comparison of all the modeled SEDs obtained from the fixed grid of parameters used for the modeling. First, each model is scaled and normalized to the data by minimizing χ^2. Then the

[14] https://cigale.lam.fr/

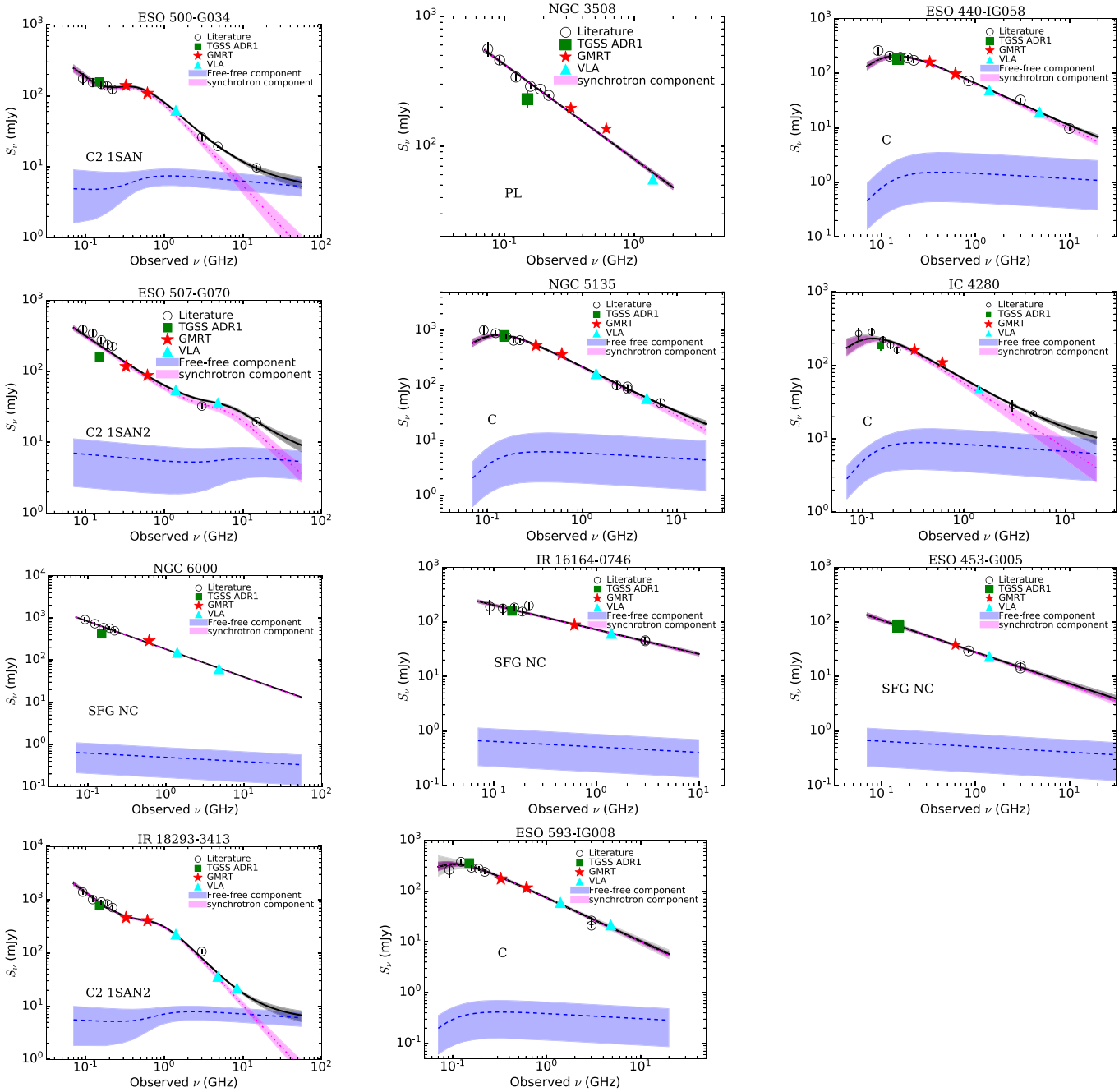

Figure 1. Radio SED for our sample of LIRGs. Galaxy name and the best-fit radio SED model name are provided at the top and inside each panel. The solid black line represents the best-fit model, while the gray shaded region represents the 1σ uncertainties sampled by the UltraNest package. The dotted–dashed magenta and dotted blue lines show the decomposed synchrotron and free–free components. The pink and blue shaded regions represent the 1σ uncertainties in the synchrotron and free–free components, respectively. For galaxies fitted with two-component models, the free–free and synchrotron components correspond to the sum of individual free–free and synchrotron components. The flux density measurements obtained with GMRT (365 and 610 MHz) are shown by the filled red star symbol, while the archival VLA data that were reduced and analyzed by us (1.4, 4.8, 8.4, and 14.9 GHz) are shown by the filled cyan triangle. The filled green square indicates the TGSS ADR1 150 MHz fluxes, and the open circle represents the flux density measurements taken from the literature (GLEAM, SUMSS, NVSS, VLASS, ATCA, and Effelsberg telescope) (see Section 3.1, Table A2).

probability that a given model matches the data is quantified by the likelihood taken as $e^{-\chi^2/2}$. These likelihoods can then be used as weights to estimate the physical parameters (the likelihood-weighted means of the physical parameters) and the related uncertainties (the likelihood-weighted standard deviation of the physical parameters). Finally, models with low probability are discarded, leaving only the best models to determine the physical parameters. Due to this process, the calculated uncertainties are symmetric (see also, Section 4.3 of Boquien et al. 2019). This method of choosing the best-fit model also takes care of the degeneracies in the model parameters, as only one parameter value (one with the highest probability in the probability distribution function (PDF)) can result in the best-fit SED.

Next, we provide a brief account of the selected models used in our study. The first step toward obtaining the SED model

requires building the stellar emission, which consists of selecting the single stellar population model (in our case; Bruzual & Charlot 2003), assuming a Salpeter (1955) initial mass function. Next, to model the SFH, we adopted a delayed SFR with an additional burst profile (in accordance with Małek et al. 2018). This form of SFH provides good estimates of the SFR–$M_\star$ relation compared to observations (Ciesla et al. 2015). The SFH is defined as

$$\mathrm{SFR}(t) \propto \begin{cases} \mathrm{SFR}_{\mathrm{delayed}}(t)\text{: if } t < t_0. \\ \mathrm{SFR}_{\mathrm{delayed}}(t) + \mathrm{SFR}_{\mathrm{burst}}(t), \text{ :if } t \geqslant t_0. \end{cases} \quad (11)$$

where t_0 is the age since the onset of the second episode (burst) of star formation.

To model starlight attenuation by dust, we chose the extinction law of Calzetti et al. (2000), and to model dust emission, we selected The Heterogeneous Evolution Model for Interstellar Solids (THEMIS; Jones et al. 2017) model. THEMIS successfully explains the observed FUV to near-IR extinction and the shape of the IR to millimeter dust thermal emission. Furthermore, it predicts the observed relationship between the $E(B-V)$ color excess and the inferred submillimeter opacity derived from Planck observation (for information see Jones et al. 2017; Nersesian et al. 2019). To incorporate the AGN component in the SED, we selected the SKIRTOR module (Stalevski et al. 2012, 2016). SKIRTOR is based on the 3D radiative transfer code SKIRT (Baes et al. 2011). It includes obscuration by dusty torus and obscuration by dust settled along with the polar directions. Since our galaxies have a rich amount of radio data, we used 1.4 and 4.8 GHz fluxes to model the nonthermal synchrotron emission taking into account the PL of the synchrotron spectrum and the ratio of the FIR/radio correlation in the CIGALE fitting.

Table 3 gives the set parameters used to build the SEDs of our galaxies. We adopted parameters similar to those used in Małek et al. (2017) and Paspaliaris et al. (2021) and modified them accordingly to suit the galaxies in the current sample. The SED fitting was performed with a very careful adjustment of the fitting parameters, module by module. We performed a PDF analysis method to calculate the likelihood function (χ^2) for all possible combinations of parameters (see Section 4.3 of Boquien et al. 2019). We generate the marginalized PDF for every parameter and assess the suitability of the SED model by visual inspection. An example of this method is given in Figure 2 for the galaxy IC 4280 for dust mass. Figure 3 provides the CIGALE fit for our LIRGs. We note that some of the photometric data and the best model vary, and for them, the residuals exceed 20%–30%. We want to stress that those residuals are often related to strong emission lines, visible for the nebular model. Moreover, this kind of catalog, which includes data from different surveys and instruments, sometimes performed more than 10–20 yr ago (GALEX, XMM-OM), reduced with different reduction procedures, can result in heterogeneous photometric coverage of the spectra. In the SED fitting procedure, all measurements are treated with the same weight, and it can happen that the residuals of some of them are not as small as we would expect. The most significant residuals can be found for the g' and r' bands for our galaxies. As fits for the UV part of the spectra look very good, we can assume that the young stellar population was fitted with very good precision. The same observation can be made for i', z', and

Table 3
List of Input Parameters for CIGALE Modeling

Parameters		Values
Delayed SFH + Additional Burst (Ciesla et al. 2015)		
e-folding time of the main stellar population model [Myr]	τ_{main}	300–15,000 by a bin of 300
e-folding time of the late starburst population model [Myr]	τ_{burst}	50–1000 by a bin of 50
Mass fraction of the late burst population	f_{burst}	0.05, 0.1, 0.3, 0.6, 0.9
Age of the main stellar population in the galaxy [Myr]	age	1000, 2000, 3000, 4500, 5000, 6500, 10,000, 12,000
Age of the late burst [Myr]	$\mathrm{age}_{\mathrm{burst}}$	10.0, 40.0, 80.0, 110, 150, 170
Stellar Synthesis Population (Bruzual & Charlot 2003)		
Initial mass function	IMF	(Salpeter 1955)
Metallicity	Z	0.02
Separation age		1 Myr
Dust Attenuation Laws (Calzetti et al. 2000)		
Color excess of young stars	$E(B-V)$	0.1–2 by a bin of 0.2
Reduction factor [(iii)]	f_{att}	0.3, 0.44, 0.6,0.7
Dust Grain Model; THEMIS (Jones et al. 2017)		
Fraction of small hydro-carbon solids	q_{hac}	0.02, 0.06, 0.1,0.17, 0.24
Minimum radiation field	U_{min}	1, 5, 10, 15, 20, 30
PL index of the radiation	α	2
Fraction illuminated from U_{min} to U_{max}	γ	0.02,0.06,0.1,0.15,0.2
Active Nucleus Model; Skirtor (Stalevski et al. 2012, 2016)		
Optical depth at 9.7 μm	$\tau_{9.7}$	3.0, 7.0
Torus density radial parameter	pl	1.0
Torus density angular parameter	q	1.0
Angle between the equatorial plan and edge of the torus [deg]	oa	40
Ratio of outer to the inner radius	R	20
Fraction of total dust mass inside clumps [%]	Mcl	97
Inclination (viewing angle) [deg]	i	30 (type 1), 70 (type 2)
AGN fraction		0.0–0.4 by a bin of 0.05
Extinction law of polar dust		SMC
$E(B-V)$ of polar dust		0.01–0.7 by a bin of 0.5
Temperature of the polar dust	K	100
Emissivity index of the polar dust		1.6
Synchrotron Emission		
FIR/radio parameter[a]	q_{IR}	2.3–2.9 by a bin of 0.1
PL slope (flux $\propto$ frequency$^{\alpha_{\mathrm{synch}}}$)	α_{synch}	−1.8 to −0.2 by a bin of 0.1

Note.
[a] Computed as $\log_{10} L_{\mathrm{IR}(8-1000\mu\mathrm{m})}$ -$\log_{10} L_{1.4\,\mathrm{GHz}}$ where $L_{1.4\,\mathrm{GHz}}$ is the radio luminosity at 1.4 GHz.

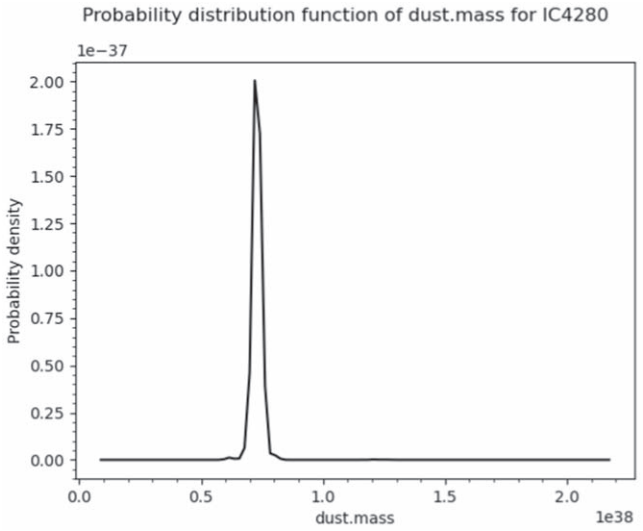

Figure 2. PDF of the estimated dust mass for galaxy IC 4280 using Bayesian inference.

near-IR measurements, which assume a good estimation of the stellar mass and properties of older stellar populations.

Another issue we want to address here is effect of different aperture sizes taken for flux measurements at different wavelengths for the SED modeling. Indeed, the apertures do not match for galaxies in our sample. The resulting SED fitting can be influenced by the decrement in the flux, especially in nearby galaxies, where the beam size can be smaller than the galaxy itself. Also, a too large aperture in the case of a smaller galaxy can result in measuring a partial flux from another nearby galaxy. In our case, we tried to use an aperture size that was adequate to the size of a galaxy. Of course, it is impossible to match it perfectly without remeasuring fluxes, as was done in Ramos Padilla et al. (2020). As expected, this uncertainty in flux measurements results in errors for different estimated physical properties. In addition, CIGALE adds a 10% error to account for all these deviations. Problems with aperture, data reduction, and normalization can be seen as *jumps* in the SED instead of a smooth transition between different measurements. However, in the case of galaxies studied in this paper, the spectral coverage with broadband photometry is dense enough to obtain realistic physical properties. For the SED fitting procedure, fluxes were used together with the accompanying error. In our CIGALE analysis, we also checked all PDFs for estimated physical properties such as stellar masses, SFR, dust mass, and dust temperature. We did not find any strange or suspicious behavior that incorrect photometric matching can trigger. We note that Ramos Padilla et al. (2020) showed that recalculating flux measurements can increase the quality of estimated astrophysical properties; however, we did not remeasure the fluxes in our analysis.

5. Results

5.1. Radio-only and FUV to Radio SED Modeling

The densely sampled radio-only and panchromatic (FUV to radio) SEDs for our sample are fitted with UltraNest and CIGALE modeling tools, respectively. Figures 1 and 3 present radio-only and FUV to radio spectral fits, respectively. Figure 4 provides Bayesian estimates of the model parameters while Table 6 provides frequentist estimates of the model parameters. Our main results are as follows:

1. The radio continuum SEDs of our galaxies covering $\sim$70 MHz- $\sim$ 15 GHz frequency range show a variety of features: (1) single PL model arising from synchrotron emission without thermal contribution, (2) single-component PL models due to synchrotron and free–free emission with and without turnover at low frequencies, and (3) two-component models with distinct emission regions, optical depths, and sometimes different spectral index of the CRe (Figure 1). The derived radio synchrotron spectral index ranges between $-0.45^{+0.03}_{-0.03}$ and $-1.74^{+0.04}_{-0.08}$. The turnover frequencies for SEDs fitted with models with absorption features fall in the range between 100^{+20}_{-20} MHz and $7.55^{+1.94}_{-1.97}$ GHz (Table 4).
2. Figure 3 provides the CIGALE fit for our LIRGs. CIGALE modeling of the galaxies provides the rest-frame IR luminosity in the wavelength range of 8–1000 μm ($\log\ {}_{10}L_{\rm IR(8-1000\mu m)}$) as 10.77 ± 0.02–11.86 ± 0.02 $L_{\odot}$. The $q_{\rm IR}$ parameter is $\sim 2.30 \pm 0.02$ to $\sim 2.67 \pm 0.05$ while the radio spectral index estimated between 1.4 and 5 GHz is in the range of $\sim -0.61 \pm 0.03$ to 1.20 ± 0.09. The range of estimated stellar mass, dust mass, and dust temperature are $\log_{10} M_{\star} = 9.51 \pm 0.08$ to $10.91 \pm 0.19\ M_{\odot}$, $\log_{10} M_{\rm dust} = 7.37 \pm 0.04$ to 8.30 ± 0.03 $M_{\odot}$, and $T_{\rm dust} = 24.16 \pm 0.02$ to 30.70 ± 0.06 K, respectively. The SFR $\log_{10}{\rm SFR_{IR}}$ is 0.31 ± 0.12 to 1.71 ± 0.16 ($M_{\odot}\ {\rm yr}^{-1}$). The AGN fraction that contributes to the optical and IR emission ranges between $1.06\% \pm 0.41\%$ and $6.10\% \pm 0.60\%$ (Table 6).
3. Including the radio measurements in CIGALE modeling allowed us to obtain better constrained $L_{\rm dust}$ values as compared to CIGALE modeling results in the literature, which did not include radio measurements. Although the dust luminosity of our galaxies falls in the range exhibited by galaxies of the same class, we note that our $L_{\rm dust}$ estimates have $\sim$1 order of magnitude lower uncertainties (0.02 dex; Table 6) than those provided in the literature ($\sim$0.2 dex; Małek et al. 2017).
4. Figure 4 shows a comparison between the $q_{\rm IR}$ estimated from the CIGALE modeling and Equation (12). The relation between these values is closer to unity and agrees within errors, with a scatter (or average deviation), $\sigma = 0.16$.
5. To cross check the robustness of the CIGALE analysis, we present a comparison of the AGN fractions obtained for eight galaxies in our sample with the AGN fractions derived by Díaz-Santos et al. (2017) in Figure 5. CIGALE computes the AGN fraction using an AGN template that contributes between UV and IR wavelengths. In contrast, Díaz-Santos et al. (2017) compute the AGN fraction using the mid-IR spectral diagnostics, including emission-line ratios, the equivalent width of 6.2 μm polycyclic aromatic hydrocarbon, the dust continuum slope at 30 and 15 μm as well as spectral template-based diagrams. The relation between these values is closer to unity and they agree within error, with a scatter, $\sigma = 0.04$. A close correspondence between our and Díaz-Santos et al. (2017) values validates the analysis procedure.
6. Figure 6 shows the computed TF vs. rest frame IR luminosity for our sample.

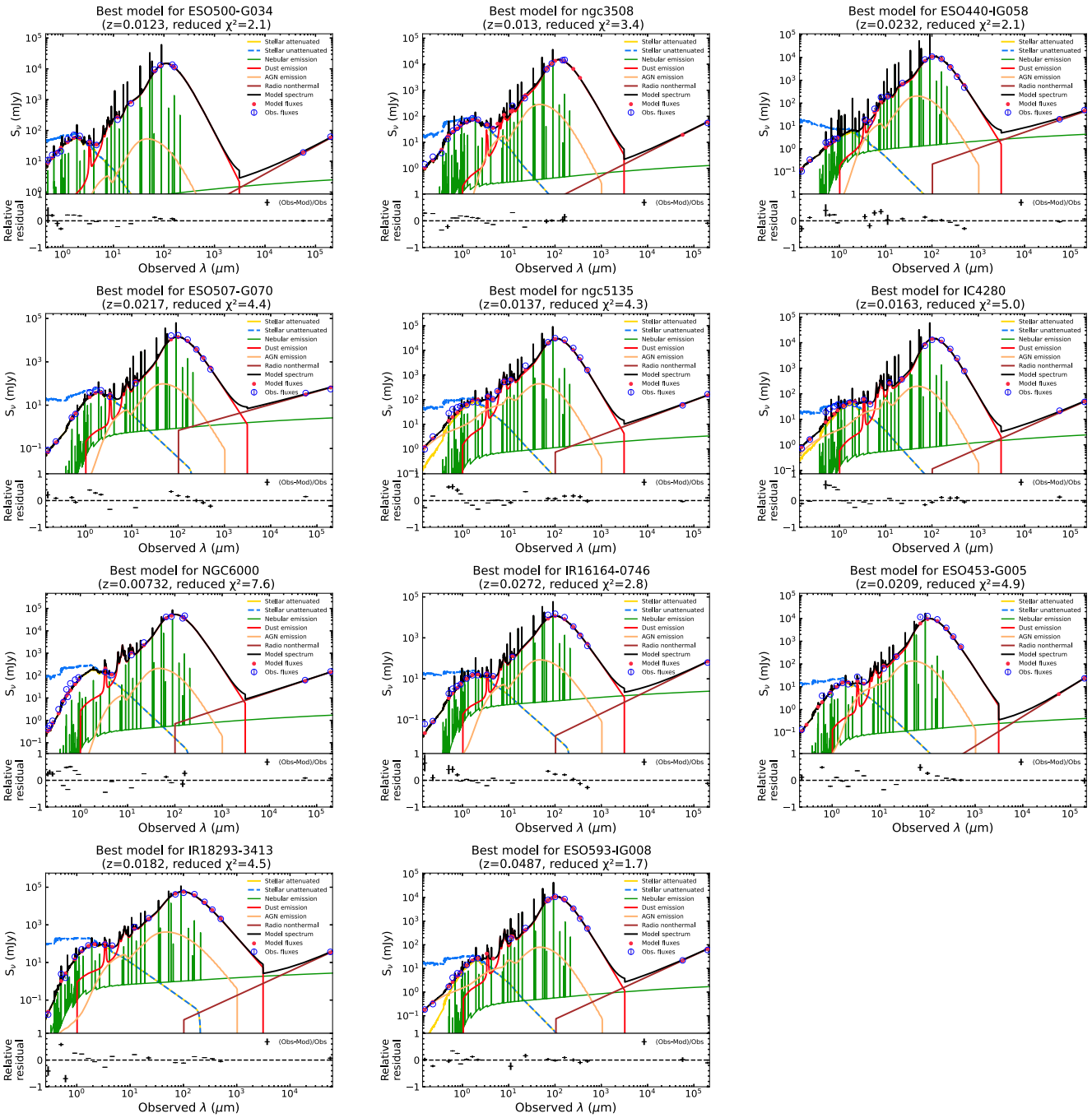

Figure 3. Best-fit CIGALE SEDs of the 11 LIRGs studied here. The open and filled symbols indicate the observed and modeled flux densities. The goodness of fit is estimated by reduced χ^2 shown at the top of each panel, along with the name and redshift of the galaxy. In almost all cases, SEDs are well modeled, giving reasonable estimates of astrophysical properties.

5.2. *Specific Results on Individual Galaxies*

1. ESO 500-G034: Classified as an intermediate between the Seyfert-type AGN nucleus and a starburst galaxy (Hill et al. 1999), the densely sampled radio spectrum covering ∼2.3 decades in frequency (70 MHz–14.9 GHz) is fitted with a two-component model representing two distinct star-forming regions where the first component is without turnover. The turnover frequency is ∼0.52 GHz. The synchrotron spectral index, $\alpha = -1.15$. The TF at 1.4 GHz is ∼11.4%. The CIGALE modeling estimates an $\mathrm{SFR_{IR}} = 5.72\,M_\odot\ \mathrm{yr}^{-1}$, high $L_{\mathrm{dust}} = 10^{11.86}\ L_\odot$, and low AGN fraction = 1.11%, respectively. The low AGN fraction obtained by our analysis contradicts the previous results by Hill et al. (1999) who classified this source as an intermediate between an AGN and a starburst galaxy (its low AGN fraction is also confirmed by Díaz-Santos et al. 2017).
2. NGC 3508: Classified as a spiral galaxy (Veilleux et al. 1995), its densely sampled radio spectrum covering 2.9 decades in frequency (70 MHz–3 GHz) is fitted with a single-component model characterized by synchrotron emission only. The synchrotron spectral index, $\alpha = -0.73$. The TF is 0 as this emission is characterized by

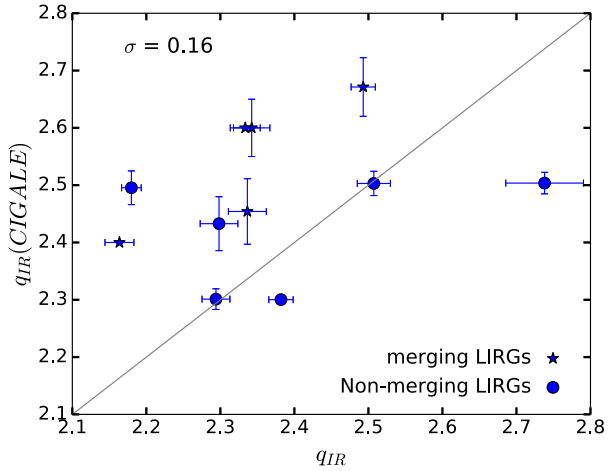

Figure 4. Comparison of $q_{\rm IR}$ estimated by CIGALE modeling and Equation (12). The gray line represents the one-to-one relation and the scatter, σ, from unity is given.

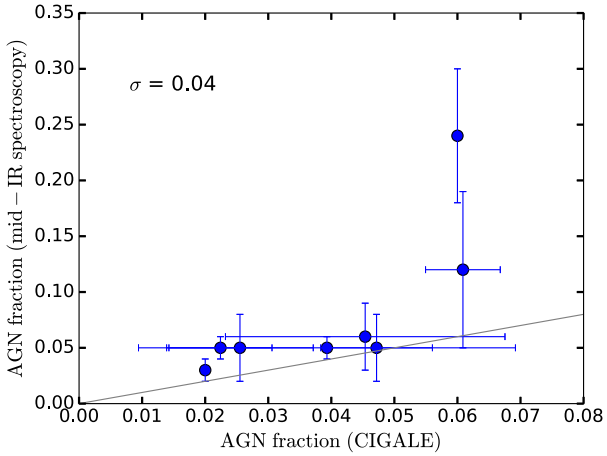

Figure 5. Comparison of bolometric AGN fractions obtained in this work and Díaz-Santos et al. (2017) for eight LIRGs in our sample. The gray line represents the one-to-one relation and the scatter, σ, from unity is given.

Table 4
The Most Preferred Models Selected on the Basis of the Bayes Odds Ratio and the Constrained Value of the Free Parameters

Name	Model	A (mJy)	B (mJy)	α	$\nu_{t,1}$ (GHz)	C (mJy)	D (mJy)	α_2	$\nu_{t,2}$ (GHz)
(1)	(2)	(3)	(4)	(5)	(6)	(7)	(8)	(9)	(10)
ESO 500-G034	C2 1SAN	$6.21^{+2.23}_{-1.83}$	$3.58^{+3.13}_{-2.48}$	$-1.18^{+0.11}_{-0.12}$	...	$154.37^{+11.53}_{-10.90}$	$3.80^{+3.20}_{-2.64}$	...	$0.52^{+0.07}_{-0.06}$
NGC 3508	PL	$62.20^{+2.55}_{-2.31}$	...	$-0.73^{+0.02}_{-0.02}$	...	...	...	...	...
ESO 440-IG058	C	$325.81^{+19.13}_{-16.75}$	$1.79^{+2.33}_{-1.28}$	$-0.82^{+0.03}_{-0.04}$	$0.14^{+0.02}_{-0.02}$	...	...	...	...
ESO 507-G070	C2 1SAN2	$39.95^{+4.46}_{-4.30}$	$5.10^{+3.25}_{-3.30}$	$-0.77^{+0.05}_{-0.06}$	...	$21.07^{+3.98}_{-4.20}$	$2.25^{+1.77}_{-1.53}$	$-1.50^{+0.38}_{-0.22}$	$7.49^{+1.85}_{-2.01}$
NGC 5135	C	$1294.29^{+80.51}_{-70.09}$	$7.34^{+8.88}_{-5.28}$	$-0.88^{+0.03}_{-0.05}$	$0.13^{+0.02}_{-0.02}$	...	...	...	...
IC 4280	C	$359.44^{+43.22}_{-30.17}$	$10.43^{+5.69}_{-5.93}$	$-0.89^{+0.09}_{-0.12}$	$0.13^{+0.03}_{-0.03}$	...	...	...	...
NGC 6000	SFG NC	$144.60^{+3.21}_{-3.26}$	$0.48^{+0.34}_{-0.32}$	$-0.66^{+0.01}_{-0.02}$	...	...	...	...	...
IR 16164-0746	SFG NC	$61.52^{+2.27}_{-2.33}$	$0.49^{+0.36}_{0.33}$	$-0.45^{+0.03}_{-0.03}$	...	...	...	...	...
ESO 453-G005	SFG NC	$22.34^{+1.06}_{-0.99}$	$0.52^{+0.32}_{-0.35}$	$-0.59^{+0.04}_{-0.04}$	...	...	...	...	...
IR 18293-3413	C2 1SAN2	$34.13^{+12.20}_{-9.91}$	$4.09^{+3.28}_{-2.75}$	$-1.33^{+0.12}_{-0.14}$	...	$373.64^{+42.37}_{-41.82}$	$4.19^{+3.08}_{-2.79}$	$-1.74^{+0.08}_{-0.05}$	$1.06^{+0.08}_{-0.09}$
ESO 593-IG008	C	$540.79^{+73.47}_{-47.65}$	$0.49^{+0.34}_{-0.34}$	$-0.87^{+0.03}_{-0.03}$	$0.10^{+0.02}_{-0.02}$	...	...	...	...

Note. The nominal value is taken as the 50th percentile of the posterior distribution of the samples, and the 1σ uncertainties are provided by the 16th and 84th percentiles. Parameters not included in the models are indicated as "...". Columns: (1) galaxy name, (2) best-fit model, (3) and (7) nonthermal normalization components, (4) and (8) thermal normalization components, (5) and (9) synchrotron spectral indices, (6) and (10) turnover frequencies.

synchrotron emission (i.e., no free–free component). The CIGALE modeling gives $\rm SFR_{IR} = 3.90\,M_\odot\ yr^{-1}$, $L_{\rm dust} = 10^{11.25}\ L_\odot$, and AGN fraction = 6.00%, respectively, for this galaxy.

3. ESO 440-IG058: Classified as a galaxy merger with a LINER-type AGN northern neighbor (Corbett et al. 2003), this galaxy is known to show shock-dominated emission for the southern system (Rodríguez-Zaurín et al. 2011). Its radio SED covering 2.1 decades (70 MHz–10.0 GHz) is fitted with single-component star-forming region properties (including absorption) with a turnover at ∼140 MHz. The synchrotron spectral index, $\alpha = -0.82$. The computed TF is 3.17%. The CIGALE-estimated $\rm SFR_{IR}$, $L_{\rm dust}$, and AGN fraction are $42.66\,M_\odot$ $\rm yr^{-1}$ and $10^{10.99}\ L_\odot$, ∼4.53%, respectively. Our $\rm SFR_{IR}$ value is comparable within uncertainty to that obtained in literature ($\sim 36\,M_\odot\ \rm yr^{-1}$; Miluzio et al. 2013) and ($\sim 48\,M_\odot\ \rm yr^{-1}$; Herrero-Illana et al. 2017).
4. ESO 507-G070: Classified as a Seyfert-type AGN nucleus (Condon et al. 1996) in a post-merger system (Stierwalt et al. 2013; Paspaliaris et al. 2021), its radio SED covering ∼2.3 decades in frequency (70 MHz–14.9 GHz) is best fitted with a two-component model representing two distinct star-forming regions with different ultrarelativistic electron populations and high-frequency turnover. The synchrotron spectral indices for the two populations, α and α_2, are −0.77 and −1.50, respectively. The TF is ∼9%. The $\rm SFR_{IR}$, $L_{\rm dust}$, and AGN fraction are $22.40\,M_\odot$ $\rm yr^{-1}$, $10^{10.93}\ L_\odot$, and ∼2.0%, respectively. Its UV-IR SED has previously been modeled with CIAGLE by Paspaliaris et al. (2021) who reported comparable $L_{\rm dust}$ ($=10^{11.1}\ L_\odot$) and $\rm SFR_{IR}$ ($45.1\,M_\odot\ \rm yr^{-1}$), and a lower AGN fraction (0%) as compared to our results.
5. NGC 5135: Classified as having a Seyfert-type AGN nucleus (Condon et al. 1996) with a strong starburst along the spiral arms (Muñoz Marín et al. 2007), its radio SED covering ∼2.0 decades in frequency (70 MHz–6.7 GHz) is fitted with single-component star-forming region properties (including absorption) with a turnover at ∼0.130 GHz. The synchrotron spectral index, $\alpha = -0.88$. The TF is

~3.6%. The CIGALE-estimated SFR_{IR}, L_{dust}, and AGN fraction are $11.22\,M_\odot$ yr^{-1}, $10^{11.21}$ $L_\odot$, and ~6%, respectively.

6. IC 4280: Classified as a spiral galaxy (Fairall et al. 1989; Jin et al. 2019), its radio SED covering ~1.6 decades (70 MHz–3.0 GHz) is best fitted with a single-component star-forming region properties (including absorption) with a turnover at ~140 MHz. The synchrotron spectral index, $\alpha = -0.9$. The TF is 11.9%. The CIGALE-estimated SFR, L_{dust} and AGN fraction are $11.75\,M_\odot$ yr^{-1}, $10^{11.36}$ $L_\odot$, and ~6%, respectively.
7. NGC 6000: Classified as a starburst galaxy (Carollo et al. 2002), its radio SED covering ~1.6 decades in frequency (70 MHz–3.0 GHz) is best fitted with emission from a single star-forming region without a low-frequency turnover. The synchrotron spectral index is −0.66. The TF is 0.3%. The CIGALE-estimated SFR, L_{dust}, and AGN fraction are $2.04\,M_\odot$ yr^{-1}, $10^{10.79}$ $L_\odot$, and ~1.06%, respectively.
8. IR 16164-0746: Classified as a late stage merger (Stierwalt et al. 2013) with a single LINER-type nucleus and a tidal tail (Dixon & Joseph 2011; Hung et al. 2015), its radio SED covering ~1.6 decades in frequency (70 MHz–3.0 GHz) is best fitted with emission from a single star-forming region without low-frequency turnover. The synchrotron spectral index is ~−0.5. The TF is 0.8%. The CIGALE-estimated SFR, L_{dust}, and AGN fraction are $33.11\,M_\odot$ yr^{-1}, $10^{10.77}$ $L_\odot$, and ~2.2%, respectively.
9. ESO 453-G005: A galaxy pair that appears to be dominated by star-forming activity, although it does not show signs of interaction (Rich et al. 2015), its poorly sampled radio SED covering ~1.3 decades in frequency (150 MHz–3.0 GHz) is best fitted with emission from a single star-forming region without a low-frequency turnover. The synchrotron spectral index is ~−0.6. The TF is 2%. The CIGALE-estimated SFR, L_{dust}, and AGN fraction are $3.31\,M_\odot$ yr^{-1}, $10^{10.97}$ $L_\odot$, and ~4.7%, respectively.
10. IR 18293-3413: A complex system, classified both as an early-merger (Haan et al. 2011) and mid-merger (Ricci et al. 2017) galaxy system with no evidence of AGN activity (X-ray spectrum; Risaliti et al. 2000), its radio SED covering ~2.1 decades in frequency (70 MHz–8.4 GHz) is best fitted with a two-component model representing two distinct star-forming regions with different ultrarelativistic CRe and one region without any turnover. The synchrotron spectral indices for the two populations are −1.33 and −1.74, respectively. The turnover frequency is 1.06 GHz. The TF is ~3.7%. The CIGALE-estimated SFR, L_{dust}, and AGN fraction are $15.48\,M_\odot$ yr^{-1}, $10^{11.7}$ $L_\odot$, and ~2.5%, respectively.
11. ESO 593-IG008: Known as the *Bird* (Väisänen et al. 2017), this system is a a well-known galaxy merger (Stierwalt et al. 2013; Hung et al. 2015). Its radio SED covering 1.8 decades (70 MHz–4.8 GHz) is fitted with a single-component star-forming region synchrotron (including absorption) with a turnover at ~100 MHz. The synchrotron spectral index, $\alpha = -0.87$. The computed TF is 0.6%. The CIGALE-estimated SFR, L_{dust}, and AGN fraction are $51.3\,M_\odot$ yr^{-1}, $10^{11.18}$ $L_\odot$, and ~3.9%, respectively.

6. Discussion

6.1. q_{IR} Parameter

We estimate q_{IR} using FIR fluxes at 60 and 100 μm and 1.4 GHz radio flux to compare with other samples in the literature (Yun et al. 2001; Galvin et al. 2018). That is, we use the following expression given by Yun et al. (2001):

$$q_{IR} \equiv \log_{10}\left(\frac{FIR}{3.75 \times 10^{12}\ W\ m^{-2}}\right) - \log_{10}\left(\frac{S_{1.4\ GHz}}{W\ m^{-2}\ Hz^{-1}}\right). \quad (12)$$

The FIR is computed using $FIR \equiv 1.26 \times 10^{-14}(2.58\,S_{60\mu m} + S_{100\mu m})$ W m^{-2} where $S_{60\mu m}$ and $S_{100\mu m}$ are the 60 and 100 μm band flux densities, in jansky, from IRAS. The error on *the* q_{IR} parameter, computed using Equation (12), is derived following standard error propagation. Figure 7 shows the distribution of $\log_{10} q_{IR}$ obtained based on Equation (12) with respect to monochromatic IR luminosity at 60 μm ($=4\,\pi\,d_L^2 \times S_{60\mu m}$ where d_L is the luminosity distance). To obtain the luminosity distance, we use the cosmological calculator[15] (Wright 2006) with the Hubble constant $H_0 = 69.6$ km s^{-1} Mpc^{-1}, $\Omega_M = 0.286$, and $\Omega_\lambda = 0.714$ (Bennett et al. 2014). In this plot, the upper and lower dashed lines represent the 3σ bounds of the mean value. The objects falling above and below the dashed lines are called the *IR excess* (upper dashed line) and the *radio excess* (lower dashed line), respectively. Our sample exhibits typical values of q_{IR}, indicating that radio emission is dominated by star-forming processes without any hint of abnormal behavior, such as AGN dominance or unusually high star-forming activity. This supports the results of our UV to IR fitting from CIGALE, where the median AGN fraction is ~2.5%, and only for one source ESO 453-G005 is close to ~10%. Furthermore, the distribution of q_{IR}, with respect to $\log_{10} L_{60\mu m}/(L_\odot)$ provides results comparable to those obtained for other LIRGs by Yun et al. (2001) and Galvin et al. (2018). According to the plot, the merging and non-merging galaxies take values from the main, most frequent range of q_{IR} values and are indistinguishable in this aspect.

6.2. TF

From the radio SED modeling, we computed the TF at 1.4 GHz, $TF_{1.4\ GHz}$, for our sample, which ranges between $0.003^{+0.002}_{-0.002}$ and $0.12^{+0.04}_{-0.04}$ (Table 5). We plot the $TF_{1.4\ GHz}$ against the rest-frame IR luminosity from CIGALE (Figure 6). Our values are similar to those obtained for a different sample of starburst galaxies, including LIRGs and ULIRGs (19 galaxies at median redshift equal to 0.09; Galvin et al. 2018). These values are also compatible with those obtained from normal star-forming galaxy samples (Niklas et al. 1997; Tabatabaei et al. 2017).

6.3. Radio Spectral Indices and Spectral Curvature

The integrated radio spectra for our sample of LIRGs show complex forms and are rarely described by single PLs (Figure 1). Eight out of 11 galaxies show bends in their spectra, which we model as arising due to FFA. Here, we mention that curvatures in radio SEDs can also occur if the

[15] http://www.astro.ucla.edu/~wright/CosmoCalc.html

Table 5
Total, Thermal and Nonthermal Fluxes Estimated at 1.4 GHz from the Radio-only SED Fitting and the Corresponding TF Estimated at 1.4 GHz

Name	$S_{1.4}^{\rm total}$ (mJy)	$S_{1.4}^{\rm th}$ (mJy)	$S_{1.4}^{\rm nth}$ (mJy)	$\rm TF_{1.4}$
(1)	(2)	(3)	(4)	(5)
ESO 500-G034	$59.74^{+1.94}_{-1.74}$	$7.32^{+1.82}_{-2.22}$	$52.57^{+3.06}_{-2.74}$	$0.11^{+0.02}_{-0.02}$
NGC 3508	$61.84^{+2.55}_{-2.42}$	...	$61.84^{+2.55}_{-2.42}$	0
ESO 440-IG058	$49.98^{+1.03}_{-1.04}$	$1.59^{+1.79}_{-1.13}$	$48.39^{+1.66}_{-2.24}$	$0.03^{+0.02}_{-0.02}$
ESO 507-G070	$53.02^{+1.59}_{-1.59}$	$4.75^{+3.41}_{-3.11}$	$48.24^{+3.31}_{-3.52}$	$0.09^{+0.04}_{-0.04}$
NGC 5135	$164.33^{+3.58}_{-3.74}$	$6.04^{+7.28}_{-4.43}$	$158.29^{+6.20}_{-9.60}$	$0.04^{+0.02}_{-0.03}$
IC 4280	$50.32^{+1.52}_{-1.73}$	$8.53^{+5.04}_{-5.17}$	$41.84^{+6.12}_{-6.24}$	$0.12^{+0.04}_{-0.04}$
NGC 6000	$146.98^{+3.07}_{-3.21}$	$0.49^{+0.35}_{-0.33}$	$146.00^{+4.00}_{-3.00}$	$0.003^{0.002}_{0.002}$
IR 16164-0746	$62.04^{+2.45}_{-2.59}$	$0.51^{+0.34}_{-0.33}$	$61.50^{+2.50}_{-2.60}$	$0.008^{+0.004}_{-0.004}$
ESO 453-G005	$23.04^{+1.35}_{-1.24}$	$0.52^{+0.33}_{-0.35}$	$22.50^{-1.40}_{+1.40}$	$0.02^{+0.01}_{-0.01}$
IR 18293-3413	$220.59^{+7.18}_{-7.23}$	$7.76^{+2.10}_{-2.15}$	$212.84^{+7.95}_{-7.75}$	$0.04^{+0.01}_{-0.01}$
ESO 593-IG008	$58.59^{+1.72}_{-1.67}$	$0.36^{+0.25}_{-0.26}$	$58.22^{+1.70}_{-1.71}$	$0.006^{+0.003}_{-0.003}$

Note. The nominal value is taken as the 50th percentile of the posterior distribution of the samples, and the 1σ uncertainties are provided by the 16th and 84th percentiles. Columns: (1) galaxy name, (2–4) total, thermal and nonthermal fluxes at 1.4 GHz, (5) TF at 1.4 GHz.

refractive index of the medium is less than unity (Tsytovitch–Razin effect; Israel & Mahoney 1990), and due to synchrotron self-absorption (SSA; Israel & Mahoney 1990). For our galaxies, the radio surface brightness (=peak flux/θ^2, where the flux is in jansky and θ is the size in arcsecond of the source; for unresolved sources, we take the synthesized beam size as the upper limit for the size) is of the order of 10^{-2} (Table A1). For the SSA mechanism to be important at 100 MHz frequencies for our sources, unreasonably high magnetic field strengths >1000 G are needed (Kellermann & Pauliny-Toth 1969). Therefore, SSA as a cause of turnover can be safely ruled out for our sample. The Razin turnover frequency is given as $20 \times n_e/B$(MHz), where n_e is the electron density (per cubic centimeter) and B is the magnetic field strength in microgauss (Ginzburg & Syrovatskii 1965). In ISM, for the typical CRe density ~1 (per cubic centimeter) (Ferrière 2001) and the typical magnetic field strength of 50 μG (Crocker et al. 2010), the Razin turnover frequency turns out to be 0.4 MHz. Therefore, we can safely rule out the Razin effect as a cause of low-frequency spectral turnover.

The synchrotron spectral index ranges between ~−0.5 and ~−1.7. The galaxies IR 16164-0746 and ESO 453-G005 have relatively flatter spectra, ~−0.5, compared to the canonical value of −0.75 (Condon 1992). For these galaxies, the spectral flattening can be ascribed to a change in the CRe spectrum (electron energy index = 2.1) because of ionization losses (Lacki et al. 2010; Ramírez-Olivencia et al. 2022). Galaxies NGC 3508, ESO 440-IG058, NGC 5135, IC 4280, NGC 6000, and ESO 593-IG080 exhibit typical values of synchrotron spectral slope, ranging between −0.7 and −0.9. The remaining three galaxies, ESO 500-G034, ESO 507-G070, and IR 18293-3413, show steeper spectral slopes ranging between −1.17 and −1.74. Interestingly, galaxies showing stepper synchrotron spectral indices are fitted with two-component emission models. On the assumption that the injection indices of the electron energies are all similar but steepen due to physical processes, we expect the radiation spectral index to change by 0.5 due to synchrotron losses (Marvil et al. 2015). Therefore, within uncertainties, our spectral indices are consistent with a typical $\alpha \sim -0.75$ and a value of $\alpha \sim -1.25$. The slightly flatter values are almost within the errors, which could be due to the complexity of the radio SED. We cannot evaluate it due to the poor spectral resolution achieved in our images. We speculate along the lines of Galvin et al. (2018) who also modeled the radio SED LIRGs that the CRe energy spectrum is intrinsically steep for these galaxies. We remark that, unlike frequent assumptions, the nonthermal spectral index is not fixed, and it changes between −0.45 and −1.75, which could be due to the influence of star formation on the energetics of CRe as discussed in Tabatabaei et al. (2017).

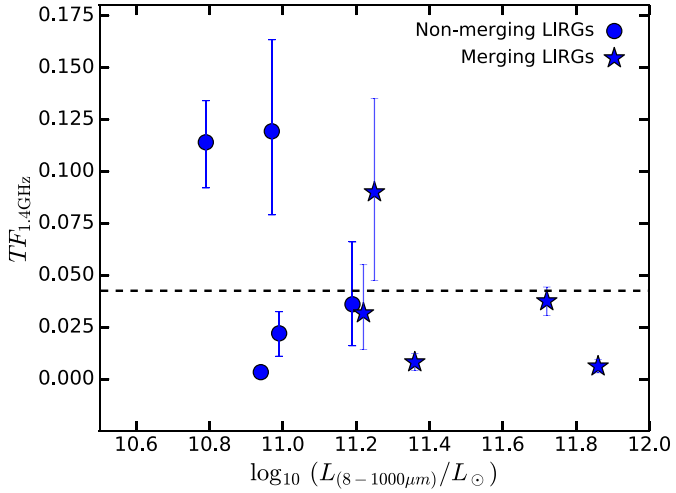

Figure 6. TF at 1.4 GHz plotted against the rest-frame IR luminosity obtained from our CIGALE modeling. The dashed line marks the average TF = 0.042 for our sample.

6.4. Emission Measure

The emission measure (EM) is an integral of the electron density along the line of sight. EM is calculated by assuming that the emission originates from a cylindrical geometry with constant temperature and electron density (Condon 1992). From the spectral turnover frequency, one can estimate the EM from the formula of the optical depth, τ_ν:

$$\tau_\nu = 3.28 \times 10^{-7} \left(\frac{T_e}{10^4\ \rm K}\right)\left(\frac{\nu}{\rm GHz}\right)^{-2.1}\left(\frac{EM}{\rm pc\ cm^{-6}}\right), \quad (13)$$

where T_e is the electron temperature of the H II emitting region and EM is the emission measure of depth s. τ_ν is the optical depth, set at unity at turnover frequency measured from our SED modeling. The EM is given by the integral of the electron density, N_e, along the line of sight of the H II region of depth s:

$$\frac{\rm EM}{\rm pc\ cm^{-6}} = \int_{\rm los}\left(\frac{N_e}{\rm cm^{-3}}\right)^2 d\left(\frac{s}{\rm pc}\right). \quad (14)$$

We compute the EMs for our sources using the turnover frequencies obtained from our modeling (Table 4) and assuming a typical electron temperature of 10^4 K (Clemens et al. 2010; Galvin et al. 2018). Table 7 provides the EMs for our sample. Our EM values cover the same range as that obtained by (19 LIRGs; Galvin et al. 2018). Furthermore, our EM values are also consistent with those obtained by Clemens et al. (2010), i.e., 20 LIRGs and ULIRGs.

Table 6
CIGALE SED Fitting Results

Name	$\log_{10}(M_\star)$ ($M_\odot$)	$\log_{10}(M_{\rm dust})$ ($M_\odot$)	$T_{\rm dust}$ (K)	$\log_{10}({\rm SFR}_{IR})$ ($M_\odot$ yr^{-1})	AGN Fraction (%)	$\alpha_{\rm synch}$	$\log_{10}(L_{\rm dust})$ ($L_\odot$)	$q_{\rm IR}$	χ^2
(1)	(2)	(3)	(4)	(5)	(6)	(7)	(8)	(9)	
ESO 500-G034	10.12 ± 0.07	7.37 ± 0.04	27.55 ± 0.42	0.72 ± 0.14	1.11 ± 0.4	-0.90 ± 0.04	11.86 ± 0.02	2.30 ± 0.01	2.1
NGC 3508	10.32 ± 0.02	7.68 ± 0.02	24.16 ± 0.02	0.59 ± 0.02	6.00 ± 0.001	-0.61 ± 0.03	11.25 ± 0.02	2.43 ± 0.04	3.4
ESO 440-IG058	9.51 ± 0.08	7.82 ± 0.02	27.24 ± 0.002	1.63 ± 0.02	4.53 ± 0.02	-1.20 ± 0.09	10.99 ± 0.02	2.60 ± 0.05	2.1
ESO 507-G070	10.79 ± 0.02	7.61 ± 0.02	30.70 ± 0.003	1.35 ± 0.02	2.00 ± 0.0004	-0.74 ± 0.08	10.93 ± 0.02	2.67 ± 0.05	4.4
NGC 5135	10.34 ± 0.03	7.89 ± 0.08	25.77 ± 1.52	1.05 ± 0.02	6.00 ± 0.04	-0.76 ± 0.09	11.21 ± 0.02	2.50 ± 0.03	4.3
IC 4280	10.44 ± 0.06	7.66 ± 0.04	27.18 ± 0.50	1.07 ± 0.02	6.10 ± 0.60	-0.96 ± 0.15	11.36 ± 0.02	2.30 ± 0.02	5.0
NGC 6000	10.32 ± 0.05	7.39 ± 0.05	28.91 ± 0.50	0.31 ± 0.12	1.06 ± 0.41	-0.90 ± 0.03	10.79 ± 0.02	2.50 ± 0.02	7.6
IR 16164-0746	10.12 ± 0.06	7.82 ± 0.02	29.21 ± 0.003	1.52 ± 0.05	2.24 ± 0.01	-0.80 ± 0.10	10.77 ± 0.02	2.45 ± 0.06	2.8
ESO 453-G005	9.62 ± 0.10	7.69 ± 0.02	27.24 ± 0.05	0.52 ± 0.20	4.72 ± 0.88	-0.82 ± 0.04	10.97 ± 0.02	2.50 ± 0.02	4.9
IR 18293-3413	10.67 ± 0.06	8.06 ± 0.02	30.70 ± 0.06	1.19 ± 0.32	2.55 ± 1.16	-1.19 ± 0.09	11.72 ± 0.02	2.60 ± 0.004	4.5
ESO 593-IG008	10.91 ± 0.19	8.30 ± 0.03	29.55 ± 0.40	1.71 ± 0.16	3.93 ± 2.7	-0.73 ± 0.68	11.18 ± 0.02	2.40 ± 0.001	1.7

Note. Columns: (1) galaxy name, (2) stellar mass, (3) dust mass, (4) dust temperature, (5) instantaneous SFR, (6) AGN fraction, (7) slope of PL synchrotron emission, α, (8) dust luminosity, (9) $q_{\rm IR}$, (10) reduced χ^2 value for the best-fit model.

Table 7
EM Derived from the Model Most Supported by the Evidence Value for Each Source

Name	EM_1 (10^6 cm^{-6} pc)	EM_2 (10^6 cm^{-6} pc)
ESO 500-G034	⋯	0.77
NGC 3508	⋯	⋯
ESO 440-IG058	0.05	–
ESO 507-G070	⋯	269.5
NGC 5135	0.04	⋯
IC 4280	0.05	⋯
NGC 6000	⋯	⋯
IR 16164-0746	⋯	⋯
ESO 453-G005	⋯	⋯
IR 18293-3413	⋯	3.44
ESO 593-IG008	0.02	⋯

Note. Sources without constrained EM are marked by "⋯".

6.5. TF versus q_{IR}

In star-forming galaxies the radio spectral index is expected to be correlated with TF and $q_{\rm IR}$ with the SFH playing a key role (Marvil et al. 2015). This is because in young star-forming galaxies ($<10^8$ yr; Condon 1992) the radio emission is mainly due to free–free emission with a relatively flatter spectrum ($\alpha \sim -0.1$) leading to relatively higher values of TF and $q_{\rm IR}$ (Marvil et al. 2015). As the starburst ages, TF and $q_{\rm IR}$ are expected to decrease as the time-delayed nonthermal emission increases with time. This is mainly because the nonthermal emission originates from relatively old ($>10^7$ yr; the average lifespan of $>8\,M_\odot$ OB type stars) relativistic electrons considering the time taken for the diffusion ($\sim 10^4$ yr) of these electrons across the galaxy is negligible (Clemens et al. 2010; Galvin et al. 2018). Figure 8 shows the relation between TF and $q_{\rm IR}$ (computed using Equation (12)) as a function of the $\rm SFR_{IR}$ ratio obtained at time intervals 10 and 100 Myr ago from the CIGALE analysis. This representation is informative in order to understand the evolution of the TF and $q_{\rm IR}$ with the age of star formation. The large scatter observed in the plot can be explained by the following reasons: (i) ceasing of star formation before nonthermal emission commences, (ii) early contribution of nonthermal emission to the radio continuum while star formation is still ongoing, and (iii) due to limited sample size.

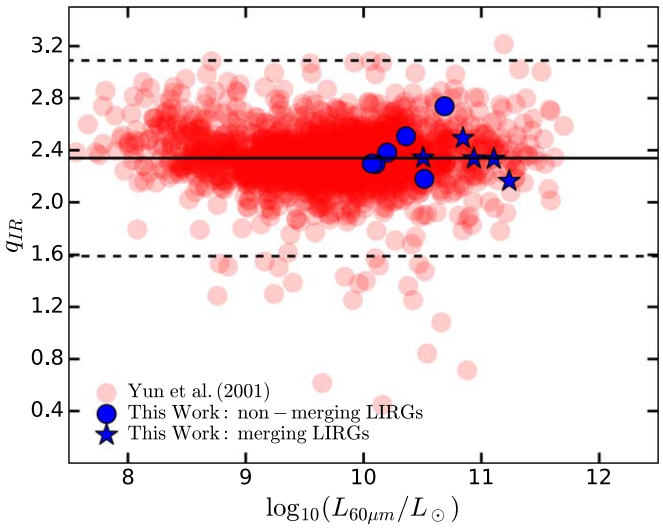

Figure 7. Distribution of $q_{\rm IR}$ with 60 μm infrared luminosity for our sample of LIRGs. The solid horizontal line marks the mean $q_{\rm IR} = 2.34$ and the dashed lines represent upper and lower 3σ bounds (Yun et al. 2001).

6.6. SFR_{IR} versus M_{dust}

In Figure 9 we show the relation of $\rm SFR_{IR}$ with dust mass for our sample, including data from the literature for normal star-forming galaxies in the Local Universe (da Cunha et al. 2010), LIRGs at low ($z < 0.5$) and high ($z > 0.5$) redshifts (Vega et al. 2008; Lo Faro et al. 2013; Pereira-Santaella et al. 2015; da Cunha et al. 2015; Małek et al. 2018; Paspaliaris et al. 2021), and ULIRGs at low and high redshifts (Vega et al. 2008; da Cunha et al. 2015; Małek et al. 2017, 2018). Our sample of LIRGs lies essentially in between the two sequences of normal and starburst galaxies defined by Rowlands et al. (2014), in excellent agreement with the behavior shown by starburst galaxies. This is because our IR selection $S_{60\mu m} \geqslant 5$ Jy selects sources to have high SFRs. Moreover, our merger-type galaxies (filled star symbol) lie systematically higher in $\rm SFR_{IR}$ than the non-mergers (filled circle) and at the same time lie systematically below the high redshift LIRGs (diamonds) and ULIRGs (plus), while the normal star-forming galaxies (cross symbol) occupy the region characterized by a lower SFR and dust mass. This can be understood as follows. With an increase

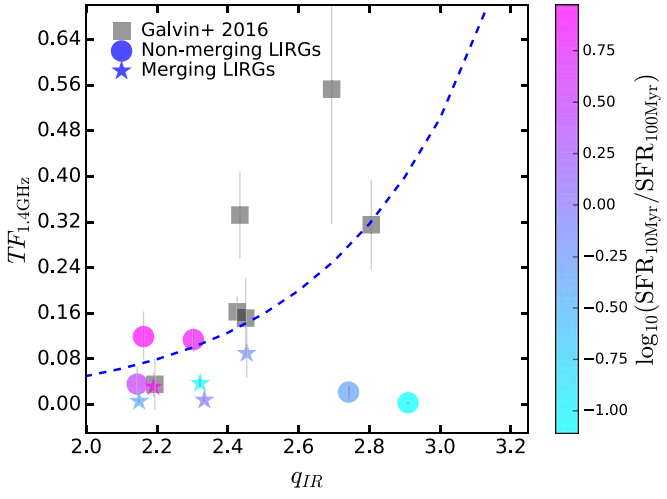

Figure 8. Distribution of TF with q_{IR} (Equation (12)) for our sample of LIRGs. The color bar indicates the SFR_{IR} obtained for a time interval of 10 Myr ago from the CIGALE analysis. The dashed line marks the relation between TF and q_{IR} given by $TF = 1.7 \times 10^{q_{IR}-3.53}$ (Marvil et al. 2015).

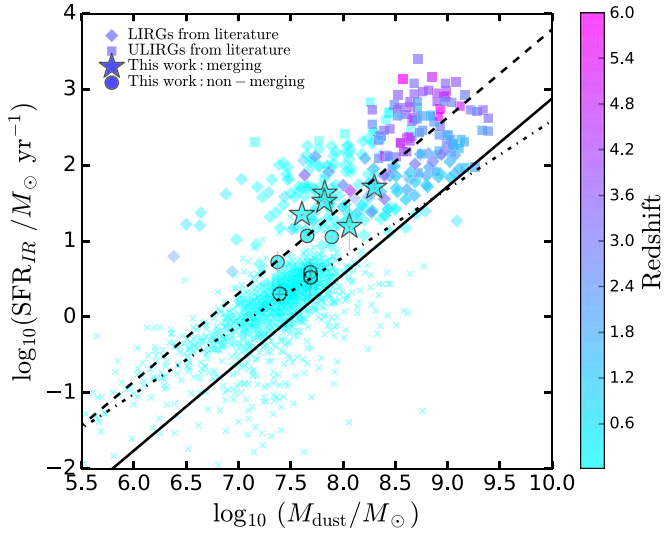

Figure 9. SFR_{IR} vs. M_{dust} for our sample of LIRGs obtained from CIGALE modeling. The solid and dashed lines, respectively, are the relations derived from low-z dusty galaxies (H-ATLAS) and starburst galaxies (local ULIRGs and $z > 2$ submillimeter galaxies) by Rowlands et al. (2014). The dotted–dashed line represents the best-fit line to the SDSS-IRAS selected local star-forming galaxies of IR luminosities ($10 \leqslant \log_{10}(L_{dust}/\ L_\odot < 12$) given by da Cunha et al. (2010).

in the SFR_{IR}, there is also an increase in the supernova rate, leading to a more efficient enrichment of the ISM with dust. Since SFR_{IR} is correlated with dust mass, and the dust relates to the gas content in galaxies (Kennicutt relation links SFR_{IR} and gas mass), therefore, a positive trend in the evolution of SFR_{IR} with dust mass is expected with our LIRGs when compared with local star-forming galaxies and ULIRGs (Rowlands et al. 2014; Donevski et al. 2020). High SFR_{IR} values are seen for interacting/merging LIRGs galaxies as compared to non-mergers (see also, Paspaliaris et al. 2021).

6.7. SFR_{IR} versus Stellar Mass and Nonthermal Fraction

Figure 10 explores the relation of stellar mass with the CIGALE-estimated SFR_{IR} for our galaxies, including the data

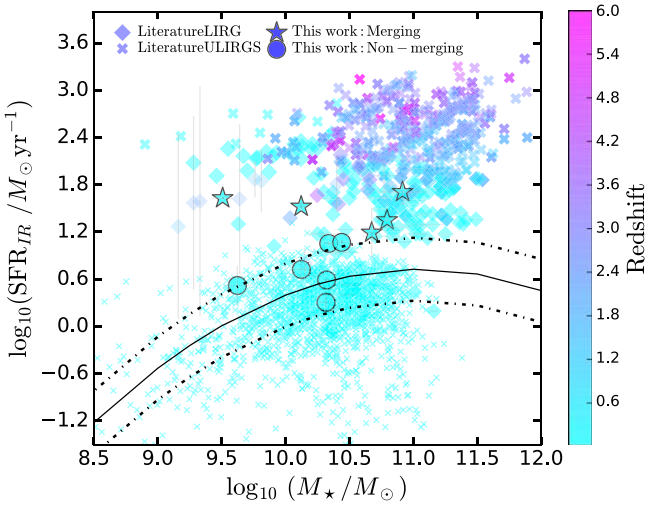

Figure 10. SFR_{IR} vs. $M_\star$ for our sample of LIRGs obtained from CIGALE modeling. The solid line represents the relation between $M_\star$ and SFR_{IR} for the main-sequence galaxies given by Schreiber et al. (2015) for a redshift range of 0.02. The dotted and dashed–dotted lines show the range of the main-sequence spreading ±0.4 dex above and below the solid line.

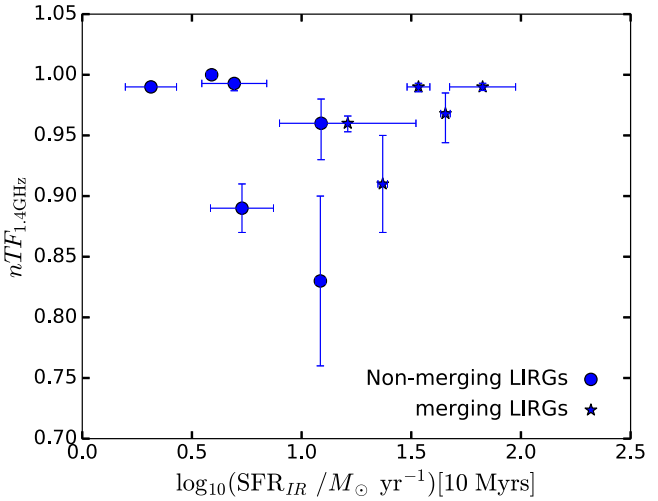

Figure 11. 1.4 GHz nTF as a function of SFR_{IR} for a time interval of 10 Myr. The nTF is estimated in the same manner as that of the TF (see Section 6.2).

for normal star-forming galaxies and the ULIRGs from the literature. As shown, our sample of LIRGs lies systematically above the main galaxy sequence represented by the parametric relation (solid line with 0.4 dex error denoted by dashed lines; Saintonge et al. 2016) along with local star-forming galaxies from the sample of da Cunha et al. (2010). There is no evidence of a correlation between stellar mass and SFR_{IR} for LIRGs and ULIRGs, including our sample (star symbol), which is explained by reaching saturation in SFR_{IR} and stellar mass for these types of galaxies (da Cunha et al. 2010; Paspaliaris et al. 2021). Figure 11 explores the relationship between the 1.4 GHz nonthermal fraction, nTF, (=nonthermal luminosity/ total luminosity), and the SFR_{IR} for our galaxy sample. All galaxies, including merger and non-merger types in our sample, exhibit high nTF values at 1.4 GHz, as expected. As we see a clear distinction between the SFR_{IR} values for merger- and non-merger-type galaxies, with the higher SFR_{IR} values being exhibited by merger-type galaxies, one would expect stronger magnetic fields B in these objects due to strong turbulence

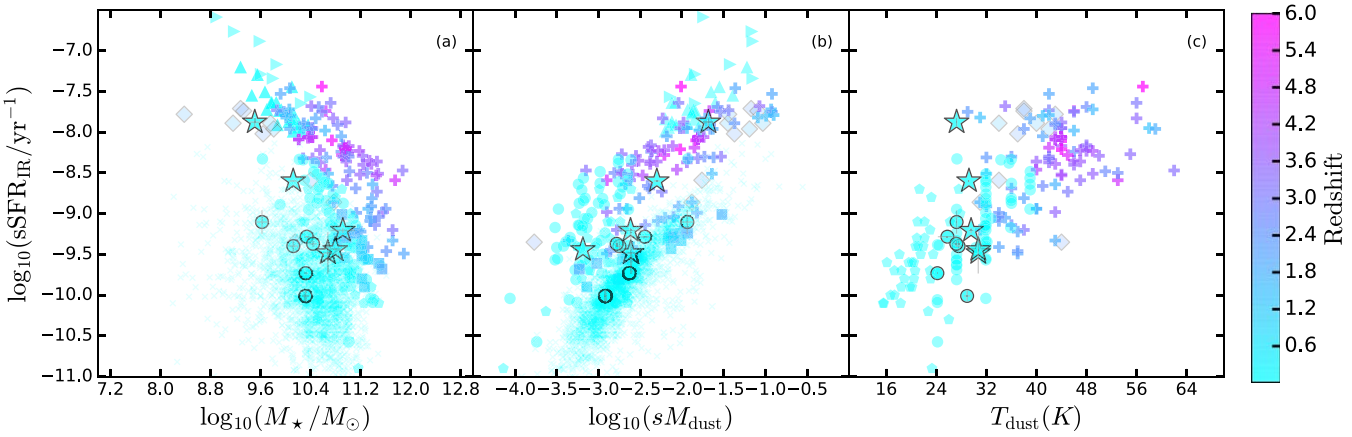

Figure 12. Distribution of $\mathrm{sSFR_{IR}}$ with respect to stellar mass (panel (a)), specific dust mass (panel (b)), and dust temperature (panel (c)) for the 11 LIRGs studied here (star and circle symbols represent the merging and non-merging types). For comparison, we include data from the literature for normal star-forming galaxies (cross; da Cunha et al. 2010), LIRGs (upward facing triangle; Vega et al. 2008), (circle; Paspaliaris et al. 2021), (diamond; da Cunha et al. 2015), (square; Lo Faro et al. 2013), and ULIRGs, (right side facing triangle; Vega et al. 2008), (plus; da Cunha et al. 2015).

created by the merger process. For a given synchrotron lifetime of CRe, $\tau_{\mathrm{synch}} \propto B^{-1.5}$, the CRe have a good chance to efficiently lose their energy via synchrotron radiation before escaping the star-forming regions.

In this regard, we note that resolved studies show that the radio spectral index is flatter in star-forming regions (Tabatabaei et al. 2007, 2013; Fletcher et al. 2011; Hassani et al. 2022), which contradicts the claimed argument of complete synchrotron cooling of CRes before escape from star-forming regions. Moreover, in star-forming regions, there is also a strong chance of CRe escape due to star formation feedback (Murphy et al. 2008). A fine balance between gas and magnetic fields/CRes can more realistically explain the nTF–$\mathrm{SFR_{IR}}$ correlation observed in normal star-forming galaxies (Tabatabaei et al. 2013; Lacki et al. 2010).

6.8. Specific SFR

Figure 12 shows the evolution of $\mathrm{sSFR_{IR}}$ (defined to be the ratio of $\mathrm{SFR_{IR}}$ and $M_\star$), with respect *to* $M_\star$ (panel (a)), specific dust mass (sM_{dust} defined to be the ratio of M_{dust} and $M_\star$; panel (b), and T_{dust} (panel (c)), respectively, for our sample of LIRGs including the data from the literature for normal star-forming galaxies along with LIRGs and ULIRGs. The $\mathrm{sSFR_{IR}}$ measures the recent star formation activity and is defined as the current star formation over the stellar mass of the galaxy (Donevski et al. 2020; Paspaliaris et al. 2021). Panel (a) shows an anticorrelation between the $\mathrm{sSFR_{IR}}$ and $M_\star$ for the three samples, indicating that massive galaxies are less efficient in star formation than less-massive ones. This is expected in the *downsizing* scenario of galaxy evolution, where massive galaxies formed most of their stars earlier and on shorter timescales. In comparison, less-massive galaxies evolve on longer timescales (Scodeggio et al. 2009; Popesso et al. 2011; Sobral et al. 2011; Laganá & Ulmer 2018).

Panel (b) shows a positive correlation between $\mathrm{sSFR_{IR}}$ and sM_{dust} for the three samples, with LIRGs and ULIRGs occupying higher $\mathrm{sSFR_{IR}}$ values per unit of specific M_{dust} compared to normal star-forming galaxies. In this plot, the contribution of $M_\star$ to $\mathrm{SFR_{IR}}$ and M_{dust} is normalized, making it ideal for studying gas-to-dust behavior in galaxies (Smith et al. 2012; Hunt et al. 2014; Donevski et al. 2020). First, the figure shows that there is an increase in dust mass compared to stellar mass on a very short timescale for these galaxies with LIRGs and ULIRGs expected to occupy the top-right corner of the plot (see Donevski et al. 2020 and references therein). The relationship between sM_{dust} and $\mathrm{sSFR_{IR}}$ indicates an evolutionary scenario where $\mathrm{sSFR_{IR}}$ decreases due to exhaustion of the gas reservoir and therefore causes an inefficient dust production, causing galaxies to occupy the bottom left corner of the plot (Burgarella et al. 2020). As expected, our LIRGs follow the trend, and local and high redshift LIRGs and ULIRGs with normal star-forming galaxies are in a different branch.

Panel (c) shows the distribution of $\mathrm{sSFR_{IR}}$ with T_{dust} for our LIRGs and local and high redshift LIRGs and ULIRGs obtained from the literature. We note that the dust temperature obtained for our LIRGs falls in a narrow range. This is most likely due to the discrete nature of the parameter space used in the CIGALE modeling, including the values provided for the interstellar radiation field needed to heat the dust (Equation (1) of Paspaliaris et al. 2021). In general, a linear trend is observed between $\mathrm{sSFR_{IR}}$ with T_{dust}, extending to high-z galaxies, which is due to the heating of dust surrounding the young stellar population in highly star-forming galaxies (Magnelli et al. 2014; Liang et al. 2019). However, our sample has more homogeneous properties and indicates dust temperature within a limited range of 24–32 K.

This comparison indicates that our galaxies fall in the middle of the parameter space occupied by normal galaxies of the Local Universe and distant starburst objects, exhibiting intermediate properties, as expected, between the two extremes of the galaxy evolution.

6.9. Calibrating SFR in Radio Wavelength

Our detailed radio SED modeling enabled us to decompose the nonthermal and thermal spectral luminosities and derive the respective SFRs. For this, we use the radio SFR calibration relations given by Murphy et al. (2011). Thermal SFR, SFR_ν^T is derived using Kroupa initial mass function (IMF; Kroupa 2001) assuming solar metallicity and continuous star formation:

$$\left(\frac{\mathrm{SFR}_\nu^T}{M_\odot\ \mathrm{yr}^{-1}}\right) = 4.6 \times 10^{-28}\left(\frac{T_\mathrm{e}}{10^4\ \mathrm{K}}\right)^{-0.45}\left(\frac{\nu}{\mathrm{GHz}}\right)^{0.1} \times \left(\frac{L_\nu^\mathrm{T}}{\mathrm{erg\ s^{-1}\ Hz^{-1}}}\right), \quad (15)$$

where L_ν^T is the thermal spectral luminosity and $T_e = 10^4$ K.

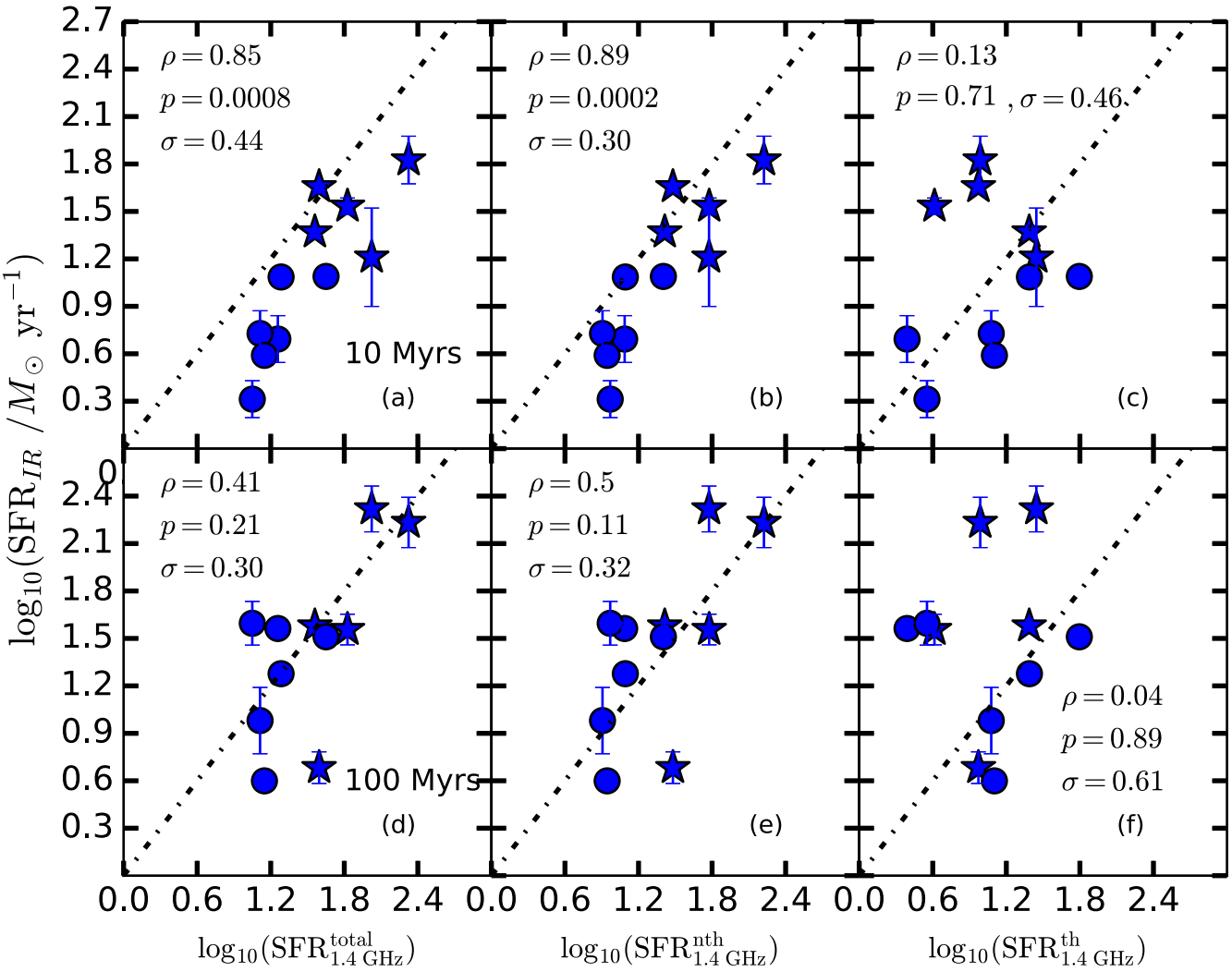

Figure 13. Comparison of the SFR_{IR} obtained for two time intervals 10 and 100 Myr ago from the CIGALE SED fitting and the 1.4 GHz radio SFR (total, nonthermal, and thermal, respectively). The mergers and non-mergers are shown with star and circle symbols, respectively. ρ-values are obtained from the application of Spearman's rank correlation test while the scatter, σ, is the average deviation from the unity.

The nonthermal SFR, SFR_ν^{NT}, is derived using calibration between the supernova rate and the SFR using the output of the Starburst99 model (Leitherer et al. 1999), and the empirical relation between supernova rate and nonthermal spectral luminosity, L_ν^{NT}, of the Milky Way (Tammann 1982; Condon & Yin 1990):

$$\left(\frac{SFR_\nu^{NT}}{M_\odot\ yr^{-1}}\right) = 6.64 \times 10^{-29}\left(\frac{\nu}{GHz}\right)^{\alpha^{NT}} \times \left(\frac{L_\nu^{NT}}{erg\ s^{-1}\ Hz^{-1}}\right), \quad (16)$$

where $\alpha^{NT} = \alpha = \alpha_{synch}$ is the synchrotron spectral index. For our calculations, we use the values obtained from the radio SED modeling (Table 4).

With the total SFR at 1.4 GHz, $SFR_{1.4GHz}$ is derived using the relation between the IR emission and current SFR resulting from the integration of the output of Starburst99 spectrum over the wavelength range of 912–3646 Å, and the q_{IR} relation (see Equation (12)). We use $q_{IR} = 2.64$ (Bell 2003) to arrive at the total $SFR_{1.4GHz}$ relation:

$$\left(\frac{SFR_{1.4\ GHz}}{M_\odot\ yr^{-1}}\right) = 6.35 \times 10^{-29}\left(\frac{L_{1.4\ GHz}}{erg\ s^{-1}\ Hz^{-1}}\right). \quad (17)$$

Figure 13 shows the comparison of the SFR_{IR} obtained from the CIGALE SED fitting for two time intervals, 10 and 100 Myr ago, and the 1.4 GHz radio SFR (total, nonthermal, and thermal, respectively). Upon visual inspection, we observe that SFR_{IR} shows a one-to-one correlation with a 1.4 GHz radio SFR, albeit with a large scatter, σ, which measures the average deviation from the unity. A striking result is that we obtain a much better correspondence of radio emission (total and synchrotron) with the young stellar population of about 10 Myr than with the older population. To check this, we applied Spearman's rank correlation test, which measures the statistical dependence between the two variables (Spearman 1904). A null hypothesis of no correlation is tested against the alternate hypothesis of non-zero correlation at a certain significance level (=0.01, adopted by us). Typically, the p-value[16] <0.01 means that the null hypothesis of no correlation is rejected at a

[16] p-value is the probability of obtaining the result as extreme as observed by chance.

confidence level >99%. For the SFR at 10 Myr ago, the obtained p-values are 0.0008 and 0.0002, respectively, rejecting the null hypothesis that the radio (total, nonthermal, and thermal) and IR SFRs are not correlated. At the same time, the ρ-values[17] are positive, indicating a positive correlation between the two variables (panels (a) and (b) of Figure 13). The null hypothesis of no correlation is not rejected for a significance level of 0.01 for thermal SFR and SFR_{IR} at 10 Myr ago (panel (c) of Figure 13) and radio and SFR_{IR} at 100 Myr ago (panels (d)–(f) of Figure 13). This is probably due to the relatively short lifetime of the CRe synchrotron at the 1.4 GHz frequency. At this frequency, in a magnetic field of about 50 μG (Crocker et al. 2010), the synchrotron lifetime is $\approx 3.3 \times 10^5$ yr. Therefore, synchrotron emission may be an effective indicator of recent SFR in galaxies. The thermal component appears to be less useful because of visible significant scatter in the predicted SFR. Since thermal emission is much weaker than synchrotron emission at this frequency, this may explain its weaker usefulness than the nonthermal component. Our analysis underlines that 1.4 GHz radio SFR measurements can be used as a diagnostic tool for high-z galaxies (Murphy et al. 2011; Tabatabaei et al. 2017).

6.10. Comparison of Radio Spectral Indices from Radio-only and CIGALE SED Modeling

We emphasize that both radio-only and FUV to radio modeling includes synchrotron emission in the models; however, the direct comparison between the synchrotron spectral index obtained from the two SED fitting techniques is inadequate. This is because the CIGALE modeling (FUV to radio) uses a very simple formulation to compute the radio flux at 1.4 GHz. This is done using the standard q_{IR} relation at 1.4 GHz and the integrated IR luminosity between 8 and 1000 μm. The radio flux at other frequencies is then computed using a single PL model with an assumed value of the spectral index. However, it is observed that the radio-only SEDs show complex morphologies (flattening or turnovers at lower frequencies and steepening at higher frequencies for some cases). Furthermore, such a direct comparison would only reveal the known scatter in the q_{IR} relation (Wang et al. 2019; Sinha et al. 2022). Furthermore, the limitations of this simple extrapolation in the CIGALE modeling are evident by the discontinuities in the radio wave bands (Figure 3).

7. Conclusion and Final Remarks

In this study, we performed joint modeling of SEDs of 11 LIRGs, focusing on radio-only and FUV to radio bands where model parameters are estimated using state-of-the-art Bayesian (radio-only) and Bayesian-like (CIGALE modeling) inference techniques. The radio-only SED modeling allowed us to decompose nonthermal and thermal radio components while the CIGALE modeling allowed us to fit complex SFH models, i.e., delayed star formation with an exponential burst (in our case), enabling us to estimate SFR_{IR} at different time intervals. Our main findings are the following:

1. The radio-only SED modeling shows that radio spectra have complex features, showing bends and turnovers. Unlike the frequent assumptions, this shows that the nonthermal spectral index is not fixed, and it changes between -0.45 and -1.75, which could be due to the influence of star formation on the energetics of CRe. The computed 1.4 GHz TF falls between $\sim$0.8% and $\sim$0.12% for our galaxies, similar to that obtained for other LIRGs in the literature.
2. Although many studies have performed FUV-IR SED modeling using CIGALE for star-forming galaxies, LIRGs, and ULIRGs (see Section 1), only a handful include radio measurements in the SED fitting (e.g., Vega et al. 2008; Shen et al. 2020; Hamed et al. 2021). The inclusion of radio measurements in the CIGALE modeling mostly serves to better constrain the derived dust luminosity. Our results indicate that, while the values of L_{IR}, fall in the range exhibited by galaxies of the same class, the uncertainties on them are improved by one order of magnitude compared to those given in the literature.
3. The $M_\star$, T_{dust}, SFR_{IR}, and AGN fraction derived using CIGALE modeling for our galaxies fall in the range exhibited by galaxies of the same class. The AGN is not energetically dominant in our sources, as the typical AGN fraction is $\leqslant$6%, similar to those found in other samples. The bolometric AGN fraction obtained by CIGALE is similar to that obtained from spectroscopic methods for most of our galaxies, indicating the robustness of the CIGALE analysis.
4. Comparison of the 1.4 GHz radio SFRs obtained using the total, and nonthermal radio emissions show a close correspondence with the CIGALE-obtained SFR_{IR} at 10 Myr ago as compared to 100 Myr ago, strengthening the view that 1.4 GHz SFR estimates are a good indicator of recent star formation.

The comparison of astrophysical properties obtained by radio-only SED modeling and CIGALE modeling with other samples studied in the literature indicates that our sample belongs to a homogeneous population of LIRGs with respect to their astrophysical properties. Finally, we end with an obvious caveat that our findings are based on a relatively small sample comprising 11 LIRGs in total and five merger-type galaxies. Therefore, a larger sample with broadband SED coverage is needed to strengthen the tentative findings presented in this study.

We thank the anonymous referee for carefully reading the manuscript and providing several constructive comments that substantially improved the content and presentation. S.D. acknowledges financial support from Jagiellonian University DSC grant N17/MNS/000014. S.D. and A.G. acknowledge support from the Polish National Science Center (NCN) through the grant 2018/29/B/ST9/02298. K.M. acknowledges support from NCN UMO-2018/30/E/ST9/00082. S.D. thanks E. da Cunha for kindly providing the data presented in da Cunha et al. (2010) in electronic form. Useful discussions with Małgorzata Bankowicz and Alexander Herzig on CIGALE analysis and Marek Jamrozy on radio data are acknowledged. We thank Krzysztof Chyży, Agnieszka Pollo, Michał Ostrowski, and Nimisha G. Kantharia for proofreading the manuscript and providing several valuable comments.

[17] ρ-value measures the strength and direction of association between two ranked variables.

We thank the staff of the GMRT that made these observations possible. GMRT is run by the National Center for Radio Astrophysics of the Tata Institute of Fundamental Research.

This research has used the NED, which is operated by the Jet Propulsion Laboratory, California Institute of Technology, under contract with the National Aeronautics and Space Administration. This research has made use of the SIMBAD database, operated at CDS, Strasbourg, France 2000, "The SIMBAD astronomical database" (Wenger et al. 2020). This research has made use of the NASA/IPAC Infrared Science Archive, which is funded by the National Aeronautics and Space Administration and operated by the California Institute of Technology. This research has made use of the VizieR catalog access tool, CDS, Strasbourg, France (DOI:10.26093/cds/vizier). The original description of the VizieR service was published in Wenger et al. (2020).

Facilities: SUMSS, GLEAM, GMRT, VLA, Effelsberg, ATCA, GALEX, XMM-OM, Swift, IRSA, Spitzer, WISE, Herschel, IRAS, Gaia, AKARI.

Software: SKIRTOR (Stalevski et al. 2012, 2016), UltraNest (Buchner 2021), CIGALE (Noll et al. 2009; Serra et al. 2011).

Appendix A
Summary of Radio Observations Gathered for Radio SED Modeling and Optical–radio Overlays

Tables A1 and A2 provide the basic information on the GMRT and VLA continuum data sets analyzed by us while Table A3 provides the integrated flux densities used in radio-only SED modeling. Figure A1 provides an overlay of the radio contours of DSS images for our galaxies. At the same time, the corner plots for the check on degeneracy on the model parameters are given in Figure A2.

Table A1
Primary and Phase Calibrators Used in Our GMRT Observations

Name	Primary (325 MHz)	Phase (325 MHz)	Primary (610 MHz)	Phase (610 MHz)
ESO 500-G034	3C 286, 3C 468.1	1130−148	3C 147, 3C 286	1130−148
NGC 3508	3C 286,3C 468.1	1130−148	3C 147, 3C 286	1130−148
ESO 440-IG058	3C 286, 3C 468.1	1248−199	3C 147, 3C 286	1248−199
ESO 507-G070	3C 286, 3C 468.1	1248−199	3C 147, 3C 286	1248−199
NGC 5135	3C 286, 3C 468.1	1248−199	3C 147, 3C 286	1248−199
IC 4280	3C 286, 3C 468.1	1248−199	3C 147, 3C 286	1248−199
NGC 6000	3C 286, 3C 468.1	1626−298	3C 147, 3C 286	1626−298
IR 16164-0746	3C 286, 3C 468.1	1626−298	3C 147, 3C 286	1626−298
ESO 453-G005	3C 286, 3C 468.1	1626−298	3C 147, 3C 286	1626−298
IR 18293-3413	3C 286, 3C 468.1	1830−360	3C 147, 3C 286	1830−360
ESO 593-IG008	3C 286, 3C 468.1	1830−360	3C 147, 3C 286	1830−360

Table A2
Summary of New GMRT and the Archival VLA Data Sets Analyzed by Us

ID	Date of Obs.	Tel.	Arr.	Frequency	BW	IF	Int.	rms	Synth. Beam	PA	S/N	Area
					(MHz)		(min)	($\frac{\text{mJy}}{\text{beam}}$)	($'' \times ''$)	(°)		(arcsec^2)
(1)	(2)	(3)	(4)	(5)	(6)	(7)	(8)	(9)	(10)	(11)	(12)	(13)
					ESO 500-G034							
23_051	2013 Jun 11	GMRT		325 MHz	32	1	32	0.78	12.49 × 7.72	33.92	142	518.9
23_051	2012 Oct 20	GMRT		610 MHz	32	1	32	0.18	6.04 × 4.27	−21.00	394	330.4
AC345	1993 May 24	VLA	CnB	1.4 GHz	50	2	2.5	0.50	25.13 × 14.66	−21.90	22	1686.8
AD229	1989 Feb 20	VLA	BnA	4.8 GHz	50	2	7.5	0.14	1.67 × 0.91	−61.11	79	11.1
AV186	1991 Mar 26	VLA	D	14.9 GHz	50	2	10.5	0.47	9.49 × 4.85	−10.96	19	113.5
					NGC 3508							
23_051	2013 Jun 11	GMRT		325 MHz	32	1	32	0.84	10.94 × 7.89	38.16	41	1703.1
23_051	2012 Oct 20	GMRT		610 MHz	32	1	32	0.31	5.63 × 4.32	−34.77	42	997.5
AC205	1988 Mar 23	VLA	C	1.4 GHz	50	3.9	2	0.90	24.98 × 16.46	−9.73	26	1729.7
					ESO 440-IG058							
23_051	2013 Jun 11	GMRT		325 MHz	32	1	32	0.60	10.94 × 7.89	38.16	41	705.9
23_051	2012 Oct 20	GMRT		610 MHz	32	1	32	0.17	7.79 × 4.20	−32.17	275	421.4
AS412	1990 Oct 6	VLA	CnB	1.4 GHz	50	2	7.9	0.28	21.50 × 11.44	−48.59	30	1147.1
AS412	1990 Oct 6	VLA	CnB	4.8 GHz	50	2	7.5	0.11	6.59 × 4.09	−44.93	92	187.1
					ESO 507-G070							
23_051	2013 Jun 11	GMRT		325 MHz	32	1	32	1.4	10.73 × 8.11	4.80	81	466.2
23_051	2012 Oct 20	GMRT		610 MHz	32	1	32	0.67	7.35 × 4.11	−43.75	190	174.5
AR531	2003 Nov 1	VLA	B	1.4 GHz	50	2	10.5	0.45	8.18 × 5.47	12.12	165	177.2
AD215	1988 Jun 9	VLA	DnC	4.8 GHz	50	2	9.3	0.15	13.69 × 12.64	−60.82	190	794.9

Table A2
(Continued)

ID	Date of Obs.	Tel.	Arr.	Frequency	BW	IF	Int.	rms	Synth. Beam	PA	S/N	Area
					(MHz)		(min)	($\frac{\text{mJy}}{\text{beam}}$)	($'' \times ''$)	(°)		(arcsec^2)
(1)	(2)	(3)	(4)	(5)	(6)	(7)	(8)	(9)	(10)	(11)	(12)	(13)
AV186	1991 Mar 26	VLA	D	14.9 GHz	50	2	10	0.52	10.10 × 4.67	−16.23	39	142.5
					NGC 5135							
23_051	2013 Jun 11	GMRT		325 MHz	32	1	32	1.8	11.96 × 7.97	4.75	558	775.0
23_051	2012 Oct 20	GMRT		610 MHz	32	1	32	0.35	7.84 × 4.13	−38.36	747	730.2
AW126	1985 Apr 1	VLA	BnA	1.4 GHz	50	2	14.6	0.23	5.22 × 3.28	49.38	10	156.1
AC351	1993 Feb 4	VLA	BnA	4.8 GHz	50	2	18.3	0.1	1.53 × 1.16	−63.68	316	34.4
					IC 4280							
23_051	2013 Jun 11	GMRT		325 MHz	32	1	32	0.59	11.95 × 8.08	9.45	99	1226.3
23_051	2012 Oct 20	GMRT		610 MHz	32	1	32	0.23	7.21 × 4.22	−39.93	99	995.6
AC345	1993 May 24	VLA	CnB	1.4 GHz	50	2	3.9	0.55	18.83 × 14.30	−48.84	56	1114.6
AD215	1988 Jun 14	VLA	DnC	4.8 GHz	50	2	8.5	0.17	13.15 × 10.61	−54.87	44	1251.0
					NGC 6000							
23_051	2012 Oct 20	GMRT		610 MHz	32	1	32	0.28	6.75 × 4.36	−17.18	600	1333.1
AC345	1993 May 24	VLA	CnB	1.4 GHz	50	2	2	0.52	27.01 × 12.43	−44.71	207	2970.5
AC326	1992 Jul 13	VLA	D	4.8 GHz	50	2	2	0.37	34.85 × 16.08	18.22	156	2828.2
					IR 16164-0746							
23_051	2012 Oct 20	GMRT		610 MHz	32	1	32	1.3	5.54 × 4.66	−17.18	152	127.8
AT149	1993 Apr 26	VLA	B	1.4 GHz	50	2	2.2	0.43	6.60 × 5.54	−0.78	137	139.7
					ESO 453-G005							
23_051	2012 Oct 20	GMRT		610 MHz	32	1	32	0.35	8.10 × 4.14	−32.73	100	227.4
AC345	1993 May 24	VLA	CnB	1.4 GHz	50	2	1.9	1.6	37.58 × 11.48	−46.21	15	798.3
					IR 18293-3413							
23_051	2013 Jun 11	GMRT		325 MHz	32	1	32	1.7	14.20 × 9.26	−5.84	423	836.7
23_051	2012 Oct 20	GMRT		610 MHz	32	1	32	1.2	13.34 × 3.98	−47.24	200	687.9
AT0	1983 Nov 30	VLA	BnA	4.8 GHz	50	2	8.5	0.21	1.03 × 0.43	8.44	23	11.1
AP534	2007 Jun 11	VLA	A	8.4 GHz	50	2	80.3	0.038	0.60 × 0.24	6.59	53	10.1
					ESO 593-IG008							
23_051	2013 Jun 11	GMRT		325 MHz	32	1	32	0.62	11.15 × 9.56	−19.53	226	667.8
23_051	2012 Oct 20	GMRT		610 MHz	32	1	32	0.34	10.19 × 4.16	−53.63	134	404.3
AT149	1993 May 23	VLA	CnB	1.4 GHz	50	2	5.2	0.68	26.66 × 12.93	33.36	75	1329.3
AF446	2007 Mar 29	VLA	D	4.8 GHz	50	2	3.6	1.1	31.22 × 22.34	−25.85	226	1452.5

Note. (1) Proposal identifier of the observation, (2) date of observations, (3) telescope used, (4) configuration array used for VLA observations, (5) central frequency of observation, (6) bandwidth used, (7) number of sub-bands used during the observation, (8) integration time used to image the target, (9) typical rms noise on the image near to the target measured using TVSTAT, (10) synthesized beam achieved, (11) position angle of the restoring beam, measured counterclockwise from the standard north direction, (12) signal to noise (S/N) ratio of the source detection (ratio of peak flux density of the source and the rms noise on the map), (12) integration area used in TVSTAT.

Table A3
Integrated Radio Flux Densities Used for the SED Fitting

Name	Obs. Freq. (GHz)	S (mJy)	Error (mJy)	Ref.
(1)	(2)	(3)	(4)	(5)
ESO 500-G034	0.091	174.25	33.06	(a)
	0.122	153.25	21.27	(a)
	0.150	155.9	24.19	(b)
	0.158	144.25	17.01	(a)
	0.189	137.5	15.39	(a)
	0.219	122.5	13.48	(a)
	0.325	139.74	7.28	(c)
	0.610	108.21	5.46	(c)
	1.4	62.61	2.23	(d)
	3.0	26.184	2.67	(e)
	4.8	19.32	0.72	(d)
	14.9	9.67	0.88	(d)
NGC 3508	.074	560	70	(f)
	0.091	459.75	34.52	(a)
	0.122	339.75	17.53	(a)
	0.150	230.0	32.8	(b)
	0.158	288.25	10.30	(a)
	0.189	274.25	7.41	(a)
	0.219	245.25	7.13	(a)
	0.325	195.80	10.66	(c)
	0.610	135.92	7.15	(c)
	1.4	55.57	2.93	(d)
	3.0	3.13	0.41	(e)
ESO440-IG058	0.091	260.75	40.56	(a)
	0.122	205.5	28.18	(a)
	0.150	156	23.07	(b)
	0.158	195.5	21.70	(a)
	0.189	190.25	20.78	(a)
	0.219	172.75	18.21	(a)
	0.325	160.01	8.23	(c)
	0.610	97.36	4.92	(c)
	0.843	72.1	5.7	(g)
	1.4	49.795	1.64	(d)
	3.0	32.32	3.22	(e)
	4.8	19.71	0.68	(d)
	10.0	9.7	0.9	(h)
ESO 507-G070	0.091	389.25	54.62	(a)
	0.122	344	40.52	(a)
	0.150	160.0	23.56	(b)
	0.158	276.5	30.61	(a)
	0.189	238.75	29.15	(a)
	0.219	224.25	24.04	(a)
	0.325	117.14	6.90	(c)
	0.610	87.79	4.75	(c)
	1.4	55.12	1.93	(d)
	3.0	32.44	3.26	(e)
	4.8	36.3	1.15	(d)
	14.9	19.37	1.17	(d)
NGC 5135	0.091	1011.25	173.16	(a)
	0.122	890.25	91.63	(a)
	0.150	826.8	83.7	(b)
	0.158	777.50	78.90	(a)
	0.189	649.75	67.38	(a)
	0.219	663.25	66.80	(a)
	0.325	533.40	27.29	(c)
	0.610	370.32	18.61	(c)
	1.40	165.69	5.03	(d)
	2.31	100.00	17.20	(i)
	3.0	95.766	9.794	(e)
	4.80	58.51	1.82	(d)
	6.70	48.00	7.20	(j)
IC 4280	0.091	271.50	49.90	(a)
	0.122	283.75	35.56	(a)
	0.150	186.1	27.54	(b)
	0.158	222.75	25.13	(a)
	0.189	189.15	22.93	(a)
	0.219	162.00	17.45	(a)
	0.325	162.4	8.46	(c)
	0.610	109.63	5.68	(c)
	1.4	48.04	1.92	(d)
	3.0	28.183	4.87	(e)
NGC 6000	0.092	913	105.53	(a)
	0.122	727.75	77.61	(a)
	0.150	418.2	59.55	(b)
	0.158	586.25	61.00	(a)
	0.189	569.75	58.18	(a)
	0.220	494	50.05	(a)
	0.61	287.03	14.51	(c)
	1.4	153.32	7.86	(d)
	4.8	62.70	2.10	(d)
IR 16164-0746	0.091	191.25	58.92	(a)
	0.122	176.50	37.05	(a)
	0.150	151.5	21.88	(b)
	0.158	183.75	26.98	(a)
	0.189	154.75	22.18	(a)
	0.219	200.25	30.21	(a)
	0.61	88.17	5.49	(c)
	1.4	62.36	3.26	(d)
	3.0	44.12	4.45	(e)
ESO 453-G005	0.15	81.6	12.67	(b)
	0.61	38.21	2.17	(c)
	0.84	29.40	2.9	(g)
	1.40	23.39	2.55	(d)
	3.00	14.28	1.45	(e)
IR 18293-3413	0.091	1390	152.79	(a)
	0.122	1006.75	107.71	(a)
	0.150	780.4	111.26	(b)
	0.158	907	92.79	(a)
	0.189	832.25	84.61	(a)
	0.219	710.25	72.27	(a)
	0.325	458.96	23.45	(c)
	0.610	405.18	20.84	(c)
	1.4	226.8	10.56	(k)
	3	106.53	10.81	(e)
	4.8	36.58	2.18	(d)
	8.4	22.09	1.16	(d)
ESO 593-IG008	0.092	261.45	71.30	(a)
	0.122	379.5	53.73	(a)
	0.150	250.0	36.07	(b)
	0.158	289.5	34.07	(a)
	0.189	277.5	30.62	(a)
	0.220	240	25.86	(a)
	0.325	174.46	8.90	(c)
	0.61	116.29	5.93	(c)
	1.4	60.35	2.36	(d)
	3.0	20.867	2.23	(e)
	4.8	21.86	1.91	(d)

Note. Columns: (1) source name; (2) observing frequency; (3) integrated flux density of the source (4) the error in the flux density including the absolute calibration uncertainty (Section 3.1), (5) references (a) GLEAM, (b) TGSS ADR1 (Intema et al. 2017), (c) current observations, (d) reanalyzed VLA, (e) VLASS (Gordon et al. 2021), (f) VLSSr (Lane et al. 2014), (g) SUMSS, (h) ATCA, (i) S-PASS (Meyers et al. 2017), (j) Effelsberg (Impellizzeri et al. 2008), (k) NVSS.

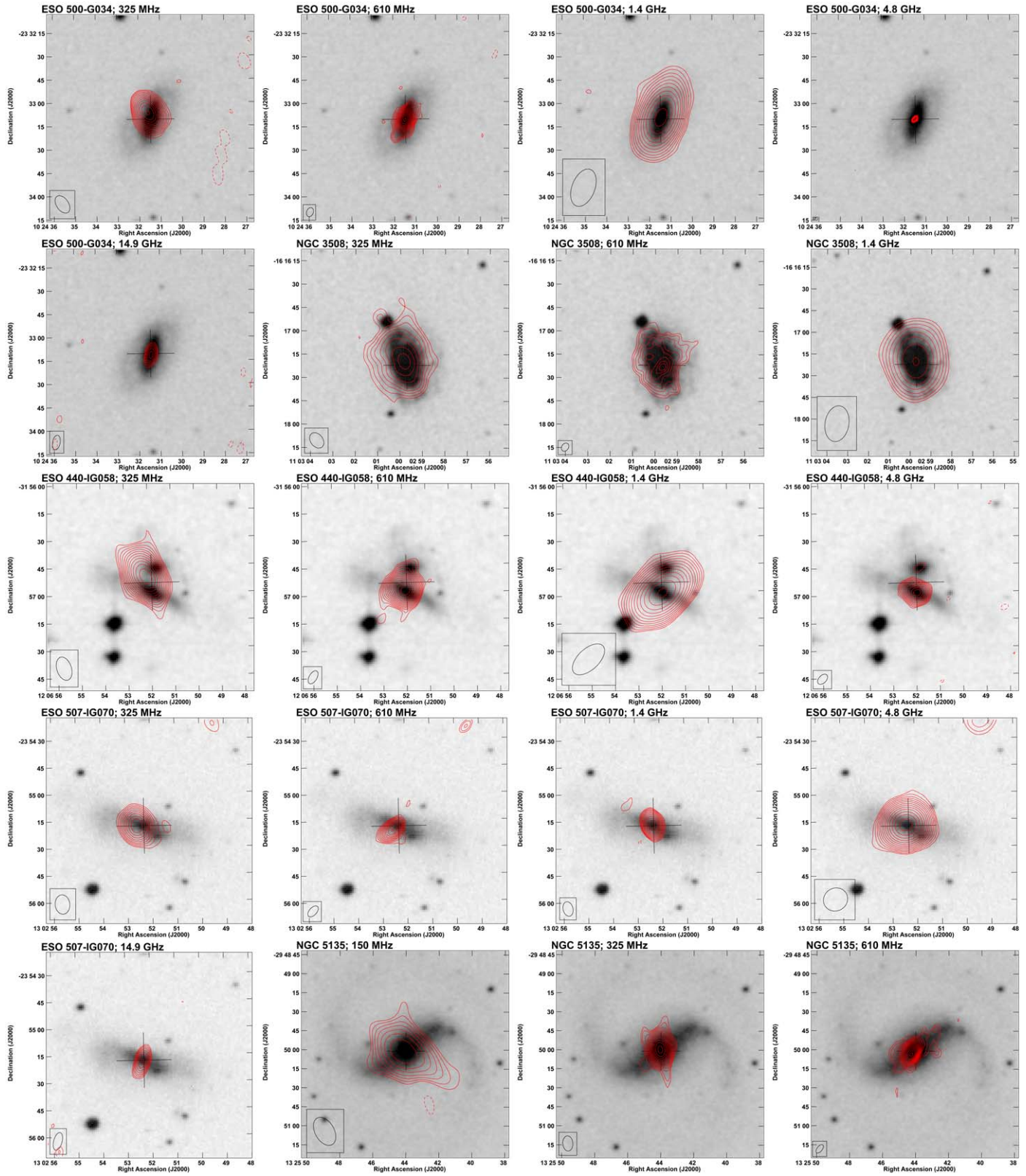

Figure A1. 150 MHz–15 GHz radio contour images (red) overlaid on the optical DSS2 *R*-band images (grayscale) for the samples of 11 LIRGs analyzed by us. The radio contours begin at 3σ of the rms noise on the radio map (Column 8 of Table A2) and increase by $(\sqrt{2})^n$ where n ranges from 0,1, 2,..20. The -3σ radio intensity is shown by dashed contours and the synthesized beam achieved is given at the bottom left corner of the image.

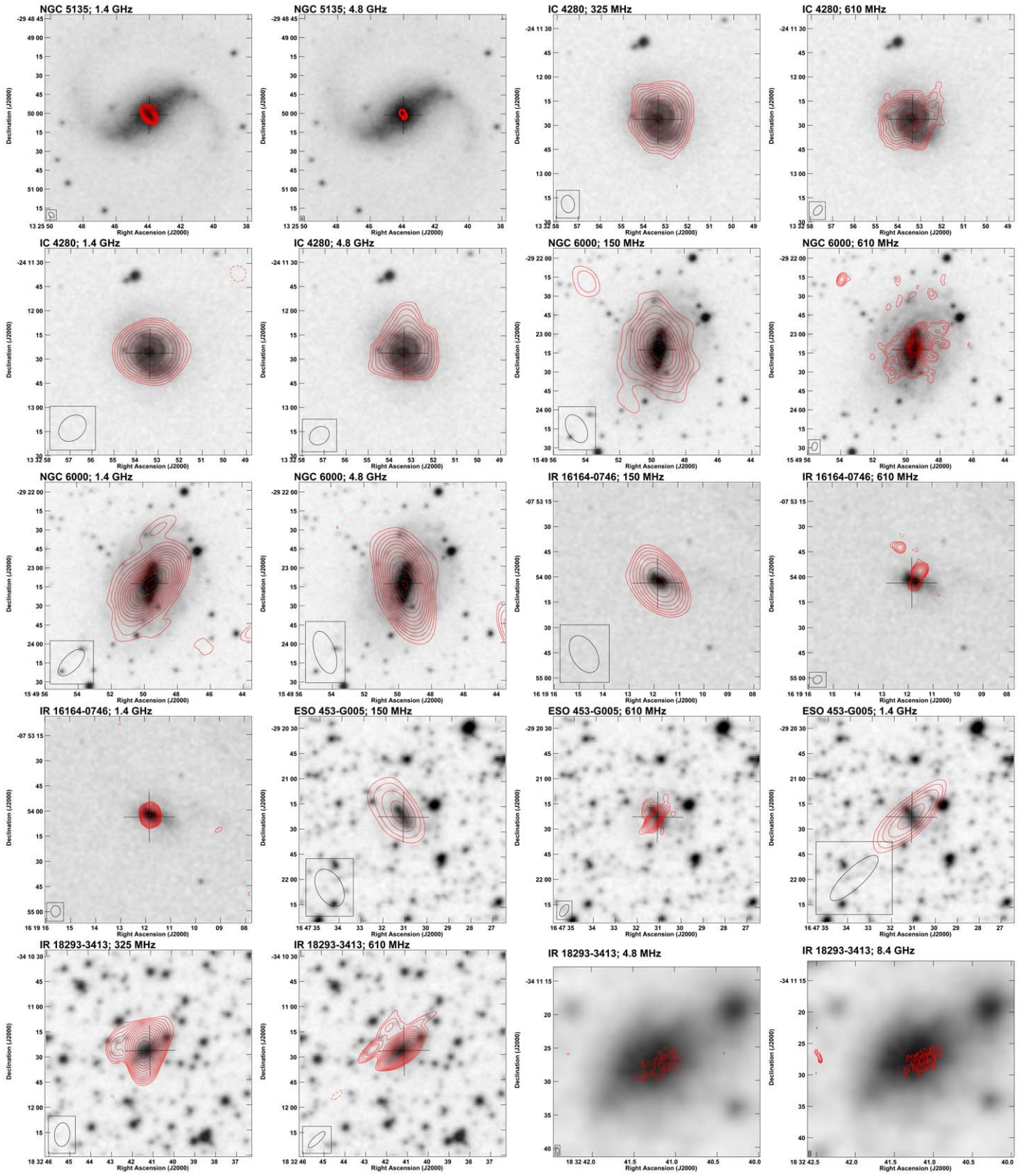

Figure A1. (Continued.)

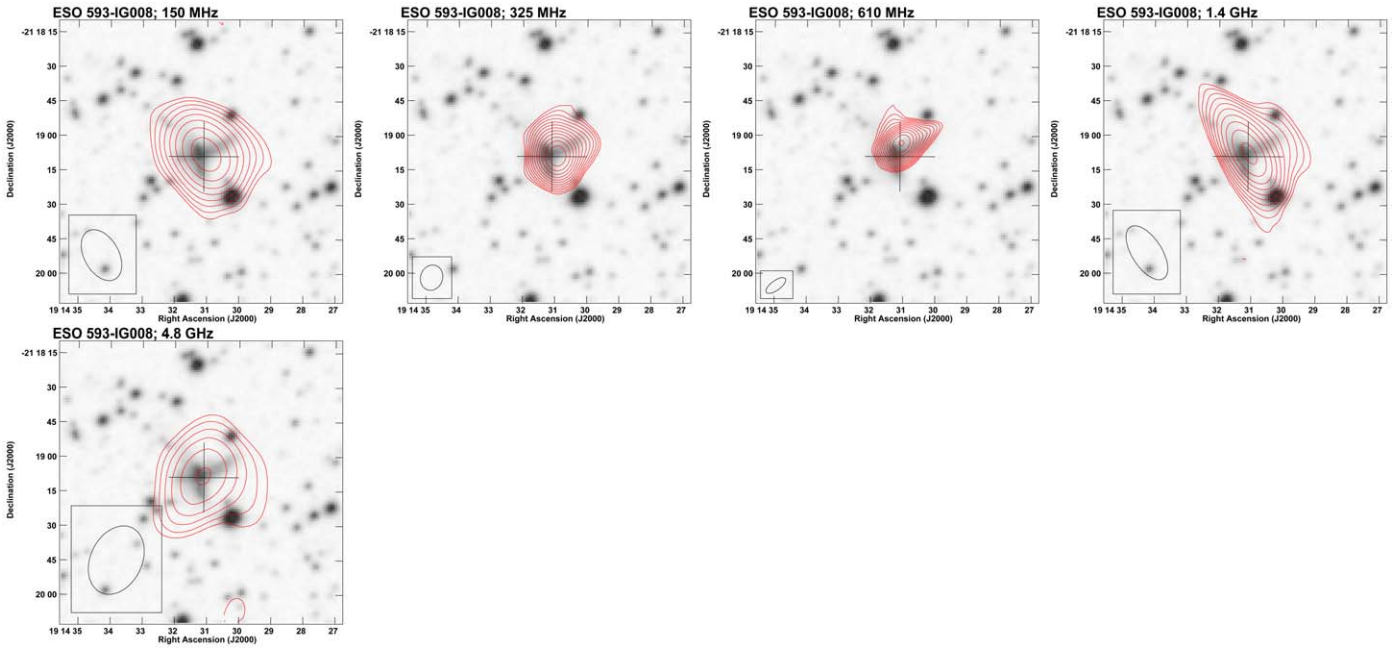

Figure A1. (Continued.)

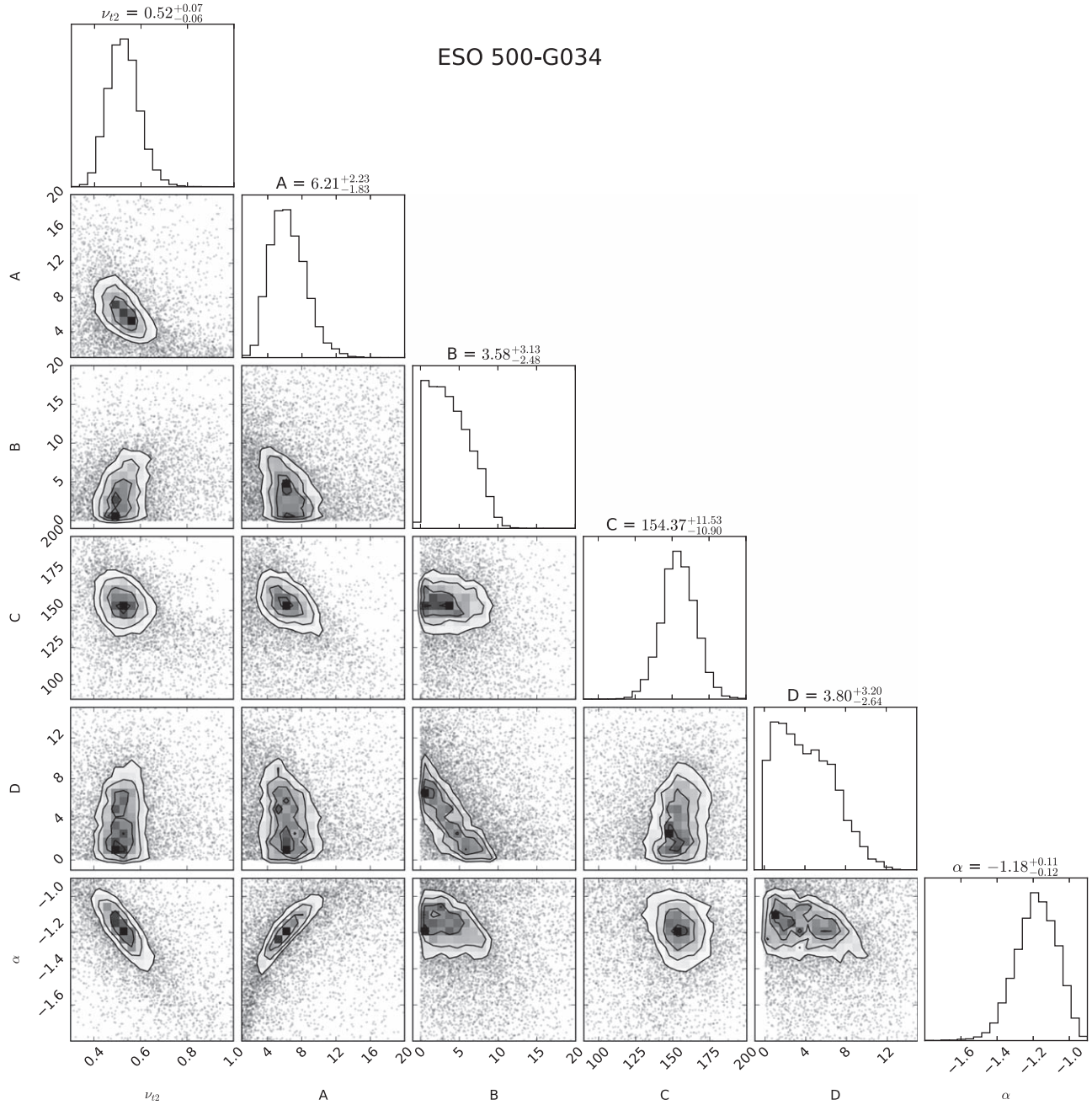

Figure A2. Corner plots showing the one and two-dimensional posterior probability distribution of the estimated parameters in the radio SED modeling for LIRG ESO 500-G034. The complete figure set (11 images) is available in the online journal.

(The complete figure set (11 images) is available.)

Appendix B
Summary of UV-IR Observations Gathered for SED Modeling via CIGALE

Table B1 lists the basic information on the instruments used for gathering multiwavelength FUV-IR data sets and Table B2 lists the flux densities used in CIGALE modeling.

Table B1
Basic Information on the Instruments/Satellites Used for UV-IR Measurements in the CIGALE Modeling

Instrument	Passbands	Central Wavelength (μm)	Resolution ($''$)
(1)	(2)	(3)	(4)
GALEX[a]	FUV, NUV	0.15, 0.227	4.2, 5.3
XMM-OM[b]	UVW2, UVW1	0.212, 0.291	1.98, 2
Swift[c]	UVW2, UVM2, UVW1,	0.193, 0.225, 0.260,	
Swift[c]	u, b, v	0.346, 0.439, 0.547	2.5 (at 350 nm)[o]
SMSS[d]	u, v, g, r, i, z	0.35, 0.38, 0.51, 0.62, 0.78, 0.92	3.1, 2.9, 2.6, 2.4, 2.3, 2.3
SDSS DR16[e]	u', g', r', i', z'	0.354, 0.477, 0.623, 0.762, 0.913	1.53, 1.44, 1.32, 1.26, 1.29
2MASS[f]	J, H, Ks	1.235, 1.662, 2.15	2
WISE[g]	W1-W4	3.4, 4.6, 12, 22	6.1, 6.4, 6.5, 12
Spitzer-IRAC[h]	IRAC1—IRAC4	3.56,4.52,5.73,7.91	1.66, 1.72, 1.88, 1.98
IRAS[i]	IRAS1—IRAS4	12, 25, 60, 100	45, 45, 90, 180
AKARI[j,k]	N60, WIDE-S, WIDE-L, N160	65, 90, 140, 160	37,39,58,61
Herschel-PACS[l]	Blue, green, red	70, 100, 160	6, 7, 12
Herschel-SPIRE[m,n]	PSW, PMW, PLW	250, 350, 500	17.9, 24.2, 35.4

Notes. Columns: (1) name of the instrument/satellite (references for the instrument are given as superscript).
[a] Bianchi & Team (1999).
[b] Mason et al. (2001).
[c] (Poole et al. 2008).
[d] (Wolf et al. 2018).
[e] https://www.sdss.org/dr16/imaging/other_info/
[f] Jarrett et al. (2000).
[g] Wright et al. (2010).
[h] Fazio et al. (2004).
[i] Neugebauer et al. (1984).
[j] Murakami et al. (2007).
[k] Doi et al. (2015).
[l] Poglitsch et al. (2010).
[m] Griffin et al. (2010).
[n] Smith et al. (2017), (2) name of the passband/filter used for observation, (3) central wavelength of the passband, and (4) resolution (FWHM).
[o] https://swift.gsfc.nasa.gov/about_swift/uvot_desc.html.

Table B2
Integrated UV-IR Flux Densities Used for the SED Fitting

Name	Instrument	Passband	S (mJy)	Error (mJy)	Integration Area (arcsec^2)	Ref.
(1)	(2)	(3)	(4)	(5)	(6)	(7)
ESO 500-G034	SMSS	g'	10.9	3.2	3.3×3.3 ″	(a)
		r'	16	0.9	$3\farcs3 \times 3\farcs3$	(a)
		i'	18.2	2.1	$3\farcs3 \times 3\farcs3$	(a)
		z'	21.3	1	$3\farcs3 \times 3\farcs3$	(a)
	2MASS	J	52.6	0.88	$55\farcs6 \times 26\farcs7$	(b)
		H	72.4	1.69	$55\farcs6 \times 26\farcs7$	(b)
		Ks	66.3	1.86	$55\farcs6 \times 26\farcs7$	(b)
	WISE	W1	40.0	0.22	$22'' \times 22''$	(c)
		W2	33.7	0.18	$22'' \times 22''$	(c)
		W3	223	1.23	$22'' \times 22''$	(c)
		W4	756	4.18	$22'' \times 22''$	(c)
	AKARI	N60	9430	350	$40'' \times 50''$[b]	(d)
		WIDE-S	13100	400	$40'' \times 50''$[b]	(d)
		WIDE-L	13700	500	$70'' \times 90''$[b]	(d)
		N160	11400	600	$70'' \times 90''$[b]	(d)
NGC3508	GALEX	FUV	1.44	0.04	$3\farcs5 \times 3\farcs5$	(e)
		NUV	2.8	0.02	$3\farcs5 \times 3\farcs5$	(e)
	SDSS	g'	13.7	1.08	$22\farcs9 \times 22\farcs9$	(f)
		r'	28	0.1	$22\farcs9 \times 22\farcs9$	(f)
		i'	36.4	0.1	$22\farcs9 \times 22\farcs9$	(f)
		z'	51.7	0.1	$22\farcs9 \times 22\farcs9$	(f)
	2MASS	J	69.2	1.29	$60\farcs4 \times 33\farcs8$	(b)
		H	81.2	2.06	$60\farcs4 \times 33\farcs8$	(b)
		Ks	72.8	2.52	$60\farcs4 \times 33\farcs8$	(b)
	WISE	W1	45.5	0.21	$22'' \times 22''$	(c)
		W2	31.8	0.175	$22'' \times 22''$	(c)
		W3	254	1.41	$22'' \times 22''$	(c)
		W4	495	3.19	$22'' \times 22''$	(c)
	AKARI	N60	6347	493	$42'' \times 42''$[b]	(d)
		WIDE-S	10690	486	$42'' \times 42''$[b]	(d)
		WIDE-L	14229	1450	$60'' \times 60''$[b]	(d)
		N160	14740	1620	$60'' \times 60''$[b]	(d)
ESO 440-IG058	GALEX	FUV	0.18	0.02	$4\farcs63 \times 4\farcs63$	(e)
		NUV	0.45	0.01	$3\farcs5 \times 3\farcs5$	(e)
	SMSS	g	1.88	0.43	$7\farcs5 \times 7\farcs5$	(a)
		r	2.00	0.11	$7\farcs5 \times 7\farcs5$	(a)
		i	2.74	0.09	$7\farcs5 \times 7\farcs5$	(a)
		z	2.83	0.08	$7\farcs5 \times 7\farcs5$	(a)
	IRAC	IRAC1	18.75	1.8		(g)
		IRAC2	14.62	1.4		(g)
		IRAC3	56.63	5.6		(g)
		IRAC4	182.56	18		(g)
	IRAS	IRAS1	200	38	$0\farcm8 \times > 0\farcm8$[a]	(h)
		IRAS2	760	35	$0\farcm8 \times > 0\farcm8$[a]	(h)
	Herschel-PACS	Blue	7972	363	$35'' \times 35''$	(i)
		Green	10620	480	$35'' \times 35''$	(i)
		Red	8597	380	$35'' \times 35''$	(i)
	Herschel-SPIRE	PSW	3371	203	$50'' \times 50''$	(i)
		PMW	1278	79	$50'' \times 50''$	(i)
		PLW	489	30	$50'' \times 50''$	(i)
ESO 507-G070	GALEX	FUV	0.09	0.01	$3\farcs5 \times 3\farcs5$	(e)
		NUV	0.21	0.01	$3\farcs5 \times 3\farcs5$	(e)
	SMSS	g'	2.72	0.14	$3\farcs55 \times 3\farcs55$	(a)
		r'	3.98	0.05	$3\farcs55 \times 3\farcs55$	(a)
		i'	6.42	0.09	$3\farcs55 \times 3\farcs55$	(a)
	2MASS	J	16.7	0.18	$14'' \times 14''$	(b)
		H	23.6	0.31	$14'' \times 14''$	(b)
		Ks	23.4	0.30	$14'' \times 14''$	(b)
	WISE	W1	24.7	0.14	$22'' \times 22''$	(c)
		W3	104	0.58	$22'' \times 22''$	(c)
	Herschel-PACS	Blue	16320	750	$43'' \times 43''$	(i)
		Green	16900	770	$43'' \times 43''$	(i)

Table B2
(Continued)

Name	Instrument	Passband	S (mJy)	Error (mJy)	Integration Area (arcsec^2)	Ref.
(1)	(2)	(3)	(4)	(5)	(6)	(7)
		Red	10660	470	$43'' \times 43''$	(i)
	Herschel-SPIRE	PSW	3747	228	$55'' \times 55''$	(i)
		PMW	1405	87	$55'' \times 55''$	(i)
		PLW	451	29	$55'' \times 55''$	(i)
NGC 5135	GALEX	FUV	0.97	0.01	$3\farcs5 \times 3\farcs5$	(e)
		NUV	3.16	0.01	$3\farcs5 \times 3\farcs5$	(e)
	SMSS	g'	27.9	1.7	$3\farcs83 \times 3\farcs83$	(a)
		r'	40.6	3.9	$3\farcs83 \times 3\farcs83$	(a)
		i'	48.7	3.6	$3\farcs83 \times 3\farcs83$	(a)
		z'	54.5	1.5	$3\farcs83 \times 3\farcs83$	(a)
	2MASS	J	59.8	0.832	$14'' \times 14''$	(b)
		H	79.9	1.11	$14'' \times 14''$	(b)
		Ks	76.7	1.14	$14'' \times 14''$	(b)
	IRAC	IRAC1	131.9	1.3		(g)
		IRAC2	103.9	1.3		(g)
		IRAC3	219.9	2.1		(g)
		IRAC4	521.9	5.2		(g)
	IRAS	IRAS1	630	35	$0\farcm8 \times > 0\farcm8$[a]	(h)
	Herschel-PACS	Blue	21440	1070	$70'' \times 70''$	(i)
		Green	31120	1560	$70'' \times 70''$	(i)
		Red	26860	1340	$70'' \times 70''$	(i)
	Herschel-SPIRE	PSW	12370	810	$100'' \times 100''$	(i)
		PMW	5058	333	$100'' \times 100''$	(i)
		PLW	1577	106	$100'' \times 100''$	(i)
IC 4280	GALEX	FUV	0.71	0.02	$3\farcs5 \times 3\farcs5$	(e)
		NUV	1.62	0.02	$3\farcs5 \times 3\farcs5$	(e)
	SMSS	g'	18.9	3.1	$3\farcs36 \times 3\farcs36$	(a)
		r'	25.3	0.4	$3\farcs36 \times 3\farcs36$	(a)
		i'	32.4	0.7	$3\farcs36 \times 3\farcs36$	(a)
		z'	37.5	0.8	$3\farcs36 \times 3\farcs36$	(a)
	2MASS	J	33.8	0.19	$14'' \times 14''$	(b)
		H	44.1	0.244	$14'' \times 14''$	(b)
		Ks	39.7	0.33	$14'' \times 14''$	(b)
	WISE	W1	58.9	0.27	$22'' \times 22''$	(c)
		W2	39.3	0.22	$22'' \times 22''$	(c)
		W3	281	1.55	$22'' \times 22''$	(c)
		W4	365	2.35	$22'' \times 22''$	(c)
	Herschel-PACS	Blue	7647	383	$45'' \times 45''$	(i)
		Green	12970	650	$45'' \times 45''$	(i)
		Red	12520	630	$45'' \times 45''$	(i)
	Herschel-SPIRE	PSW	5631	369	$65'' \times 65''$	(i)
		PMW	2431	150	$65'' \times 65''$	(i)
		PLW	771	48	$65'' \times 65''$	(i)
NGC 6000	SWIFT-UVOT	W2	0.432	0.02	$4\farcs85 \times 4\farcs85$	(j)
		M2	0.578	0.02	$5\farcs00 \times 5\farcs00$	(j)
		W1	0.959	0.04	$6\farcs25 \times 6\farcs25$	(j)
		U	3.13	0.12	$4\farcs35 \times 4\farcs35$	(j)
		B	6.41	0.26	$5\farcs40 \times 5\farcs40$	(j)
		V	11.3	0.45	$5\farcs85 \times 5\farcs85$	(j)
	SMSS	g'	24.3	0.9	$3\farcs58 \times 3\farcs58$	(a)
		r'	44.6	1.6	$3\farcs58 \times 3\farcs58$	(a)
		i'	65.8	1.1	$3\farcs58 \times 3\farcs58$	(a)
		z'	82.5	10.2	$3\farcs58 \times 3\farcs58$	(a)
	WISE	W1	145	0.80	$22'' \times 22''$	(c)
		W2	106	0.58	$22'' \times 22''$	(c)
		W3	827	4.57	$22'' \times 22''$	(c)
		W4	3010	16.6	$22'' \times 22''$	(c)
	AKARI	N60	41889	2010	$42'' \times 42''$‡	(d)
		WIDE-S	43500	963	$42'' \times 42''$‡	(d)
		WIDE-L	36169	4030	$60'' \times 60''$‡	(d)
		N160	47470	4950	$60'' \times 60''$‡	(d)
IR 16164-0746	GALEX	FUV	0.024	0.002	$3\farcs5 \times 3\farcs5$	(e)

Table B2
(Continued)

Name	Instrument	Passband	S (mJy)	Error (mJy)	Integration Area (arcsec^2)	Ref.
(1)	(2)	(3)	(4)	(5)	(6)	(7)
		NUV	0.07	0.01	$4\farcs8 \times 3\farcs5$	(e)
	SMSS	g'	1.91	0.33	$3\farcs2 \times 3\farcs2$	(a)
		r'	3.27	0.39	$3\farcs2 \times 3\farcs2$	(a)
		i'	4.44	0.28	$3\farcs2 \times 3\farcs2$	(a)
		z'	85.35	0.09	$3\farcs2 \times 3\farcs2$	(a)
	2MASS	J	10.30	0.19	$14'' \times 14''$	(b)
		H	14.90	0.276	$14'' \times 14''$	(b)
		Ks	15.1	0.34	$14'' \times 14''$	(b)
	WISE	W1	58.9	0.27	$22'' \times 22''$	(c)
		W2	39.3	0.22	$22'' \times 22''$	(c)
		W3	281	1.55	$22'' \times 22''$	(c)
		W4	365	2.35	$22'' \times 22''$	(c)
	Herschel-PACS	Blue	13290	610	$40'' \times 40''$	(i)
		Green	15030	680	$40'' \times 40''$	(i)
		Red	10210	450	$40'' \times 40''$	(i)
	Herschel-SPIRE	PSW	3581	220	$60'' \times 60''$	(i)
		PMW	1266	80	$60'' \times 60''$	(i)
		PLW	407	28	$60'' \times 60''$	(i)
ESO 453-G005	GALEX	NUV	0.131	0.01	$3\farcs7 \times 3\farcs7$	(e)
	SMSS	r	4.06	0.19	$3\farcs8 \times 3\farcs8$	(a)
		z	4.68	0.12	$3\farcs8 \times 3\farcs8$	(a)
	2MASS	J	11.1	0.29	$14'' \times 14''$	(b)
		H	14.7	0.45	$14'' \times 14''$	(b)
		Ks	12.9	0.40	$14'' \times 14''$	(b)
	WISE	W1	27.6	0.25	$22 \times 22''$	(c)
		W2	16.3	0.19	$22 \times 22''$	(c)
		W3	63.3	0.7	$22 \times 22''$	(c)
		W4	209	1.7	$22 \times 22''$	(c)
	Herschel-PACS	Blue	12190	550	$35'' \times 35''$	(i)
		Green	13950	630	$35'' \times 35''$	(i)
		Red	10040	440	$35'' \times 35''$	(i)
	Herschel-SPIRE	PSW	4150	252	$55'' \times 55''$	(i)
		PMW	1635	101	$55'' \times 55''$	(i)
		PLW	575	35	$55'' \times 55''$	(i)
IR 18293-3413	XMM-OM	UVW1	0.02	0.003	$5.7''$ x $5.7''$	(k)
	SMSS	g	4.06	1.21	$3.9'' \times 3.9''$	(a)
		r	9.19	0.43	$3.9'' \times 3.9''$	(a)
		z	19.9	0.2	$3.9'' \times 3.9''$	(a)
		Ks	12.9	0.40	$14'' \times 14''$	(b)
	2MASS	J	49.8	0.28	$14'' \times 14''$	(b)
		H	80.70	0.37	$14'' \times 14''$	(b)
		Ks	88.4	0.33	$14'' \times 14''$	(b)
	WISE	W1	88.3	0.50	$22'' \times 22''$	(c)
		W2	78.2	0.43	$22'' \times 22''$	(c)
		W3	761	3.51	$22'' \times 22''$	(c)
		W4	2270	126	$22'' \times 22''$	(c)
	Herschel-PACS	Blue	45710	2110	$50'' \times 50''$	(i)
		Green	59130	2710	$35'' \times 35''$	(i)
		Red	45840	2070	$35'' \times 35''$	(i)
	Herschel-SPIRE	PSW	17220	1070	$70'' \times 70''$	(i)
		PMW	6454	400	$70'' \times 70''$	(i)
		PLW	1987	122	$70'' \times 70''$	(i)
ESO 593-IG008	GALEX	FUV	0.166	0.01	$3.5'' \times 3.5''$	(e)
		NUV	0.30	0.01	$3\farcs5 \times 3\farcs5$	(e)
	SMSS	g	1.69	0.12	$2\farcs8 \times 2\farcs8$	(a)
		r	4.07	0.1	$2\farcs8 \times 2\farcs8$	(a)
		i	6.23	0.15	$2\farcs8 \times 2\farcs8$	(a)
		z	6.15	0.07	$2\farcs8 \times 2\farcs8$	(a)
	2MASS	J	14	0.5	$24\farcs5 \times 24\farcs5$	(b)
		H	25.2	1.0	$24\farcs5 \times 24\farcs5$	(b)
		Ks	27.1	1.2	$24\farcs5 \times 24\farcs5$	(b)
	IRAS	IRAS1	180	25	$0\farcm8 \times > 0\farcm8$[†]	(h)
		IRAS2	510	38	$0\farcm8 \times > 0\farcm8$[a]	(h)

Table B2
(Continued)

Name	Instrument	Passband	S (mJy)	Error (mJy)	Integration Area (arcsec^2)	Ref.
(1)	(2)	(3)	(4)	(5)	(6)	(7)
	Herschel-PACS	Blue	7972	363	$40'' \times 40''$	(i)
		Green	10620	480	$40'' \times 40''$	(i)
		Red	8597	380	$40'' \times 40''$	(i)
	Herschel-SPIRE	PSW	3371	203	$50'' \times 50''$	(i)
		PMW	1278	79	$50'' \times 50''$	(i)
		PLW	489	30	$50'' \times 50''$	(i)

Notes. Columns: (1) source name; (2) instrument; (3) passband; (4) total flux densities of the source; (5) the error in the flux densities; (6) integration area used in aperture photometry in terms of length of semimajor axis $a \times$ length of semiminor axis b (for circular apertures, semimajor axis = semiminor axis).
[a] Source is flagged as resolved or marginally resolved in Sanders et al. (2003).
[b] FWHM of the 2D Gaussian used in profile fitting photometry; (7) references (a) Wolf et al. (2018), (b) 2MASS Extended Mission Data Release (Skrutskie et al. 2006) (c) Wright et al. (2010); Mainzer et al. (2011), (d) Kawada et al. (2007) (e) https://galex.stsci.edu/GR6/?page=mastform, (f) The 16th Data Release of the Sloan Digital Sky Surveys (Ahumada et al. 2020), (g) For a discussion on IRAC flux estimation, see Section 3.2, (h) (Sanders et al. 2003), (i) Chu et al. (2017), (j) Yershov (2014), and (k) Page et al. (2012).

ORCID iDs

Subhrata Dey https://orcid.org/0000-0002-4679-0525
Arti Goyal https://orcid.org/0000-0002-2224-6664
Katarzyna Małek https://orcid.org/0000-0003-3080-9778
Timothy J. Galvin https://orcid.org/0000-0002-2801-766X
Nicholas Seymour https://orcid.org/0000-0003-3506-5536
Vassilis Charmandaris https://orcid.org/0000-0002-2688-1956

References

Ahumada, R., Prieto, C. A., Almeida, A., et al. 2020, ApJS, 249, 3
Baars, J. W. M., Genzel, R., Pauliny-Toth, I. I. K., & Witzel, A. 1977, A&A, 500, 135
Baes, M., Verstappen, J., De Looze, I., et al. 2011, ApJS, 196, 22
Bell, E. F. 2003, ApJ, 586, 794
Bennett, C. L., Larson, D., Weiland, J. L., & Hinshaw, G. 2014, ApJ, 794, 135
Bianchi, L. & GALEX Team 1999, MmSAI, 70, 365
Boquien, M., Burgarella, D., Roehlly, Y., et al. 2019, A&A, 622, A103
Briggs, D. S. 1995, AAS Meeting, 187, 112.02
Bruzual, G., & Charlot, S. 2003, MNRAS, 344, 1000
Buchner, J. 2021, JOSS, 6, 3001
Burgarella, D., Nanni, A., Hirashita, H., et al. 2020, A&A, 637, A32
Calzetti, D., Armus, L., Bohlin, R. C., et al. 2000, ApJ, 533, 682
Carollo, C. M., Stiavelli, M., Seigar, M., de Zeeuw, P. T., & Dejonghe, H. 2002, AJ, 123, 159
Chu, J. K., Sanders, D. B., Larson, K. L., et al. 2017, ApJS, 229, 25
Chyży, K. T., Jurusik, W., Piotrowska, J., et al. 2018, A&A, 619, A36
Ciesla, L., Elbaz, D., & Fensch, J. 2017, A&A, 608, A41
Ciesla, L., Charmandaris, V., Georgakakis, A., et al. 2015, A&A, 576, A10
Clemens, M. S., Scaife, A., Vega, O., & Bressan, A. 2010, MNRAS, 405, 887
Clemens, M. S., Vega, O., Bressan, A., et al. 2008, A&A, 477, 95
Cohen, A. S., Lane, W. M., Cotton, W. D., et al. 2007, AJ, 134, 1245
Condon, J. J. 1992, ARA&A, 30, 575
Condon, J. J., Cotton, W. D., Greisen, E. W., et al. 1998, AJ, 115, 1693
Condon, J. J., Helou, G., Sanders, D. B., & Soifer, B. T. 1996, ApJS, 103, 81
Condon, J. J., Helou, G., Sanders, D. B., & Soifer, B. T. 1990, ApJS, 73, 359
Condon, J. J., & Yin, Q. F. 1990, ApJ, 357, 97
Conroy, C. 2013, ARA&A, 51, 393
Corbett, E. A., Kewley, L., Appleton, P. N., et al. 2003, ApJ, 583, 670
Crocker, R. M., Jones, D. I., Melia, F., Ott, J., & Protheroe, R. J. 2010, Natur, 463, 65
da Cunha, E., Eminian, C., Charlot, S., & Blaizot, J. 2010, MNRAS, 403, 1894
da Cunha, E., Walter, F., Smail, I. R., et al. 2015, ApJ, 806, 110
Díaz-Santos, T., Armus, L., Charmandaris, V., et al. 2017, ApJ, 846, 32
Dixon, T. G., & Joseph, R. D. 2011, ApJ, 740, 99
Doi, Y., Takita, S., Ootsubo, T., et al. 2015, PASJ, 67, 50
Donevski, D., Lapi, A., Małek, K., et al. 2020, A&A, 644, A144
Efstathiou, A., & Rowan-Robinson, M. 2003, MNRAS, 343, 322
Fairall, A. P., Vettolani, G., & Chincarini, G. 1989, A&AS, 78, 269
Fazio, G. G., Hora, J. L., Allen, L. E., et al. 2004, ApJS, 154, 10
Ferrière, K. M. 2001, RvMP, 73, 1031
Fletcher, A., Beck, R., Shukurov, A., Berkhuijsen, E. M., & Horellou, C. 2011, MNRAS, 412, 2396
Galvin, T. J., Seymour, N., Marvil, J., et al. 2018, MNRAS, 474, 779
Ginzburg, V. L., & Syrovatskii, S. I. 1965, ARA&A, 3, 297
Gordon, Y. A., Boyce, M. M., O'Dea, C. P., et al. 2021, ApJS, 255, 30
Griffin, M. J., Abergel, A., Abreu, A., et al. 2010, A&A, 518, L3
Haan, S., Surace, J. A., Armus, L., et al. 2011, AJ, 141, 100
Hamed, M., Ciesla, L., Béthermin, M., et al. 2021, A&A, 646, A127
Hassani, H., Tabatabaei, F., Hughes, A., et al. 2022, MNRAS, 510, 11
Helou, G., Khan, I. R., Malek, L., & Boehmer, L. 1988, ApJS, 68, 151
Helou, G., Soifer, B. T., & Rowan-Robinson, M. 1985, ApJL, 298, L7
Herrero-Illana, R., Pérez-Torres, M. Á., Randriamanakoto, Z., et al. 2017, MNRAS, 471, 1634
Hill, T. L., Heisler, C. A., Norris, R. P., Reynolds, J. E., & Hunstead, R. W. 2001, AJ, 121, 128
Hill, T. L., Heisler, C. A., Sutherland, R., & Hunstead, R. W. 1999, AJ, 117, 111
Hung, C.-L., Rich, J. A., Yuan, T., et al. 2015, ApJ, 803, 62
Hunt, L. K., Palazzi, E., Michałowski, M. J., et al. 2014, A&A, 565, A112
Hurley-Walker, N., Callingham, J. R., Hancock, P. J., et al. 2017, MNRAS, 464, 1146
Impellizzeri, C. M. V., Henkel, C., Roy, A. L., & Menten, K. M. 2008, A&A, 484, L43
Intema, H. T., Jagannathan, P., Mooley, K. P., & Frail, D. A. 2017, A&A, 598, A78
Israel, F. P., & Mahoney, M. J. 1990, ApJ, 352, 30
Jarrett, T. H., Chester, T., Cutri, R., et al. 2000, AJ, 119, 2498
Jin, J.-J., Zhu, Y.-N., Wu, H., et al. 2019, ApJS, 244, 33
Jones, A. P., Köhler, M., Ysard, N., Bocchio, M., & Verstraete, L. 2017, A&A, 602, A46
Kass, R. E., & Raftery, A. E. 1995, JASA, 90, 773
Kawada, M., Baba, H., Barthel, P. D., et al. 2007, PASJ, 59, S389
Kellermann, K. I., & Pauliny-Toth, I. I. K. 1969, ApJL, 155, L71
Kroupa, P. 2001, MNRAS, 322, 231
Lacki, B. C., Thompson, T. A., & Quataert, E. 2010, ApJ, 717, 1
Lacy, M., Baum, S. A., Chandler, C. J., et al. 2020, PASP, 132, 035001
Laganá, T. F., & Ulmer, M. P. 2018, MNRAS, 475, 523
Lane, W. M., Cotton, W. D., van Velzen, S., et al. 2014, MNRAS, 440, 327
Leitherer, C., Schaerer, D., Goldader, J. D., et al. 1999, ApJS, 123, 3
Liang, L., Feldmann, R., Kereš, D., et al. 2019, MNRAS, 489, 1397
Lo Faro, B., Franceschini, A., Vaccari, M., et al. 2013, ApJ, 762, 108
Lonsdale, C. J., Farrah, D., & Smith, H. E. 2006, in Ultraluminous Infrared Galaxies, ed. J. W. Mason (Berlin: Springer), 285
Magnelli, B., Lutz, D., Saintonge, A., et al. 2014, A&A, 561, A86
Mainzer, A., Bauer, J., Grav, T., et al. 2011, ApJ, 731, 53
Małek, K., Bankowicz, M., Pollo, A., et al. 2017, A&A, 598, A1
Małek, K., Buat, V., Roehlly, Y., et al. 2018, A&A, 620, A50
Marvil, J., Owen, F., & Eilek, J. 2015, AJ, 149, 32
Mason, K. O., Breeveld, A., Much, R., et al. 2001, A&A, 365, L36
Mauch, T., Murphy, T., Buttery, H. J., et al. 2003, MNRAS, 342, 1117

Mauch, T., Murphy, T., Buttery, H. J., et al. 2013, Vizier Online Data Catalog:, VIII/81B
Meyers, B. W., Hurley-Walker, N., Hancock, P. J., et al. 2017, PASA, 34, e013
Mhlahlo, N., & Jamrozy, M. 2021, MNRAS, 508, 2910
Miluzio, M., Cappellaro, E., Botticella, M. T., et al. 2013, A&A, 554, A127
Muñoz Marín, V. M., González Delgado, R. M., Schmitt, H. R., et al. 2007, AJ, 134, 648
Murakami, H., Baba, H., Barthel, P., et al. 2007, PASJ, 59, S369
Murphy, E. J. 2009, ApJ, 706, 482
Murphy, E. J., Condon, J. J., Schinnerer, E., et al. 2011, ApJ, 737, 67
Murphy, E. J., Helou, G., Kenney, J. D. P., Armus, L., & Braun, R. 2008, ApJ, 678, 828
NASA/IPAC 2019, NASA/IPAC Extragalactic Database (NED), doi:10.26132/NED1
Nersesian, A., Xilouris, E. M., Bianchi, S., et al. 2019, A&A, 624, A80
Neugebauer, G., Habing, H. J., van Duinen, R., et al. 1984, ApJL, 278, L1
Niklas, S., Klein, U., & Wielebinski, R. 1997, A&A, 322, 19
Noll, S., Burgarella, D., Giovannoli, E., et al. 2009, A&A, 507, 1793
Ochsenbein, F., Bauer, P., & Marcout, J. 2000, A&AS, 143, 23
Page, M. J., Brindle, C., Talavera, A., et al. 2012, MNRAS, 426, 903
Paspaliaris, E. D., Xilouris, E. M., Nersesian, A., et al. 2021, A&A, 649, 33
Pearson, W. J., Wang, L., Hurley, P. D., et al. 2018, A&A, 615, A146
Pereira-Santaella, M., Alonso-Herrero, A., Colina, L., et al. 2015, A&A, 577, A78
Pereira-Santaella, M., Alonso-Herrero, A., Santos-Lleo, M., et al. 2011, A&A, 535, A93
Pérez-Torres, M., Mattila, S., Alonso-Herrero, A., Aalto, S., & Efstathiou, A. 2021, A&ARv, 29, 2
Perley, R. A., & Butler, B. J. 2017, ApJS, 230, 7
Poglitsch, A., Waelkens, C., Geis, N., et al. 2010, A&A, 518, L2
Poole, T. S., Breeveld, A. A., Page, M. J., et al. 2008, MNRAS, 383, 627
Popesso, P., Rodighiero, G., Saintonge, A., et al. 2011, A&A, 532, A145
Ramírez-Olivencia, N., Varenius, E., Pérez-Torres, M., et al. 2022, A&A, 658, A4
Ramos Padilla, A. F., Ashby, M. L. N., Smith, H. A., et al. 2020, MNRAS, 499, 4325
Ricci, C., Bauer, F. E., Treister, E., et al. 2017, MNRAS, 468, 1273
Riccio, G., Małek, K., Nanni, A., et al. 2021, A&A, 653, 18
Rich, J. A., Kewley, L. J., & Dopita, M. A. 2015, ApJS, 221, 28
Risaliti, G., Gilli, R., Maiolino, R., & Salvati, M. 2000, A&A, 357, 13
Rodríguez-Zaurín, J., Arribas, S., Monreal-Ibero, A., et al. 2011, A&A, 527, A60
Rowlands, K., Dunne, L., Dye, S., et al. 2014, MNRAS, 441, 1017
Saintonge, A., Catinella, B., Cortese, L., et al. 2016, MNRAS, 462, 1749
Salpeter, E. E. 1955, ApJ, 121, 161
Sanders, D. B., Mazzarella, J. M., Kim, D. C., Surace, J. A., & Soifer, B. T. 2003, AJ, 126, 1607
Sanders, D. B., & Mirabel, I. F. 1996, ARA&A, 34, 749
Schreiber, C., Pannella, M., Elbaz, D., et al. 2015, A&A, 575, A74
Scodeggio, M., Vergani, D., Cucciati, O., et al. 2009, A&A, 501, 21
Serra, P., Amblard, A., Temi, P., et al. 2011, ApJ, 740, 22
Shen, L., Lemaux, B. C., Lubin, L. M., et al. 2020, MNRAS, 494, 5374
Shirley, R., Duncan, K., Campos Varillas, M. C., et al. 2021, MNRAS, 507, 129
Sinha, A., Basu, A., Datta, A., & Chakraborty, A. 2022, MNRAS, 514, 4343
Sirothia, S. K., Lecavelier des Etangs, A., Gopal-Krishna, Kantharia, N. G., & Ishwar-Chandra, C. H. 2014, A&A, 562, A108
Skilling, J. 2004, in AIP Conf. Ser., 735, Bayesian Inference and Maximum Entropy Methods in Science and Engineering: 24th Int. Workshop on Bayesian Inference and Maximum Entropy Methods in Science and Engineering, ed. R. Fischer, R. Preuss, & U. V. Toussaint (Melville, NY: AIP), 395
Skrutskie, M. F., Cutri, R. M., Stiening, R., et al. 2006, AJ, 131, 1163
Smith, D. J. B., Dunne, L., da Cunha, E., et al. 2012, MNRAS, 427, 703
Smith, M. W. L., Ibar, E., Maddox, S. J., et al. 2017, ApJS, 233, 26
Sobral, D., Best, P. N., Smail, I., et al. 2011, MNRAS, 411, 675
Spearman, C. 1904, Am. J. Psychol., 15, 72
Stalevski, M., Fritz, J., Baes, M., Nakos, T., & Popović, L. 2012, MNRAS, 420, 2756
Stalevski, M., Ricci, C., Ueda, Y., et al. 2016, MNRAS, 458, 2288
Stierwalt, S., Armus, L., Surace, J. A., et al. 2013, ApJS, 206, 1
Swarup, G. 1990, IJRSP, 19, 493
Tabatabaei, F. S., Beck, R., Krügel, E., et al. 2007, A&A, 475, 133
Tabatabaei, F. S., Schinnerer, E., Krause, M., et al. 2017, ApJ, 836, 185
Tabatabaei, F. S., Schinnerer, E., Murphy, E. J., et al. 2013, A&A, 552, A19
Tammann, G. A. 1982, in Supernovae: A Survey of Current Research, Proc. NATO Advanced Study Institute, ed. M. J. Rees & R. J. Stoneham (Dordrecht: Reidel), 371
Väisänen, P., Reunanen, J., Kotilainen, J., et al. 2017, MNRAS, 471, 2059
Vardoulaki, E., Charmandaris, V., Murphy, E. J., et al. 2015, A&A, 574, A4
Vega, O., Clemens, M. S., Bressan, A., et al. 2008, A&A, 484, 631
Veilleux, S., Kim, D. C., Sanders, D. B., Mazzarella, J. M., & Soifer, B. T. 1995, ApJS, 98, 171
Vika, M., Ciesla, L., Charmandaris, V., Xilouris, E. M., & Lebouteiller, V. 2017, A&A, 597, A51
Voelk, H. J. 1989, A&A, 218, 67
Walcher, J., Groves, B., Budavári, T., & Dale, D. 2011, Ap&SS, 331, 1
Wang, L., Gao, F., Duncan, K. J., et al. 2019, A&A, 631, A109
Wayth, R. B., Lenc, E., Bell, M. E., et al. 2015, PASA, 32, e025
Wenger, M., Ochsenbein, F., Egret, D., et al. 2000, A&AS, 143, 9
Wolf, C., Onken, C. A., Luvaul, L. C., et al. 2018, PASA, 35, e010
Wright, E. L. 2006, PASP, 118, 1711
Wright, E. L., Eisenhardt, P. R. M., Mainzer, A. K., et al. 2010, AJ, 140, 1868
Yershov, V. N. 2014, Ap&SS, 354, 97
Yun, M. S., Reddy, N. A., & Condon, J. J. 2001, ApJ, 554, 803
Żywucka, N., Goyal, A., Jamrozy, M., Ostrowski, M., & Stawarz, Ł. 2014, A&A, 563, A135